Faint but Not Forgotten. I. First Results from a Search for Astrospheres around AGB Stars in the Far-ultraviolet

Raghvendra Sahai[1] , and Benjamin Stenger[1,2]

[1] Jet Propulsion Laboratory, MS 183-900, California Institute of Technology, Pasadena, CA 91109, USA; raghvendra.sahai@jpl.nasa.gov

[2] California State University, Fullerton, CA 92831, USA

Abstract

Using the GALEX archive, we have discovered extended structures around ten asymptotic giant branch (AGB) stars (out of a total 92 searched) emitting in the far-ultraviolet (FUV) band. In all but one, we find the typical morphology expected for a spherical wind moving relative to, and interacting with, the interstellar medium (ISM) to produce an astrosphere. The exception is V Hya whose mass ejection is known to be highly aspherical, where we find evidence of its large parabolic outflows interacting with the ISM, and its collimated, extreme velocity outflows interacting with the circumstellar medium. For eight objects with relatively large proper motions, we find (as expected) that the termination-shock region lies in a hemisphere that contains the proper motion vector. Radial intensity cuts for each source have been used to locate the termination shock and the astropause's outer edge. In a few objects, the cuts also reveal faint emission just outside the astropause that likely arises in shocked ISM material. We have used these data, together with published mass-loss rates and wind expansion velocities, to determine the total mass lost and duration for each source—we find that the duration of and total mass in the shocked wind are significantly larger than their corresponding values for the unshocked wind. The combination of FUV and far-IR data on AGB astrospheres provides a unique database for theoretical studies (numerical simulations) of wind–ISM interactions. We show that a Cyclical Spatial Heterodyne Spectrometer on a small space-based telescope can provide high-resolution spectra of astrospheres to confirm the emission mechanism.

Unified Astronomy Thesaurus concepts: Stellar mass loss (1613); Asymptotic giant branch stars (2100); Ultraviolet astronomy (1736); Astrospheres (107); Stellar bow shocks (1586); Circumstellar envelopes (237); Stellar winds (1636)

1. Introduction

Most stars have winds, more or less throughout their active lives (i.e., while nuclear burning is still ongoing at their centers). The mass-loss rates and expansion speeds vary as a function of evolutionary phase and stellar mass. For example, for low-mass main-sequence (MS) stars like the Sun, the mass-loss rate is $\sim 10^{-14}$ $M_\odot$ yr^{-1}, whereas for high-mass MS stars, e.g., OB stars, the mass-loss rates are $\sim 10^{-6}$–10^{-5} $M_\odot$ yr^{-1} (O stars: e.g., Smith 2014) and $\sim 10^{-9}$ $M_\odot$ yr^{-1} (B stars: e.g., Krtička 2014). Evolved low- and intermediate- mass stars lose mass at rates of $\sim 10^{-7}$–10^{-5} $M_\odot$ yr^{-1} (e.g., Olofsson 2008), but rates can reach as high as $> 10^{-4}$ $M_\odot$ yr^{-1} in some objects.

The mass loss from stars with MS masses in the 1–8 $M_\odot$ range generally peaks during the asymptotic giant branch (AGB) evolutionary phase, when the stars are very cool ($T_{\rm eff} \lesssim 3500$ K), luminous ($L \sim 10,000 L_\odot$), and undergoing strong radial pulsations. At this stage, these stars consist of a central C+O degenerate core, surrounded by He and H shells that undergo nuclear burning, and a very large stellar envelope. The heavy mass loss, believed to be driven by radiation pressure on dust grains that condense in the cool material levitated above the photosphere as a result of pulsations, produces a dusty, molecular (H$_2$), spherical, expanding (expansion speed, $V_e \sim 5$–20 km s^{-1}), circumstellar envelope (CSE) around the AGB star. The mass loss from these stars

enriches the interstellar medium (ISM) with products of nucleosynthesis (including the biogenic elements C and N), as well as dust grains, which play a crucial role in the formation of solar systems and planets. The mass-loss rate history of these stars determines the course of their late evolution and final demise.

However, it has been a major observational challenge to trace the full history of heavy mass loss in these stars. The standard tracers of the mass-loss history from ground-based observations are (i) millimeter-wave CO line emission from gas and (ii) scattered light from dust in the CSE. Observations of atomic hydrogen (H I) from the wind, generally resulting from the photodissociation of H$_2$ in the molecular wind, are usually strongly confused by Galactic emission although it has been possible to detect H I emission for a few stars (e.g., Matthews et al. 2008, 2013, 2015). CO line emission becomes undetectable, due to photodissociation by the interstellar UV field, at radii typically $\lesssim 2 \times 10^{17}$ cm (or less) even for mass-loss rates as high as $\sim 10^{-5}$ $M_\odot$ yr^{-1} (e.g., Saberi et al. 2019; Ramstedt et al. 2020), corresponding to a mass-ejection timescale of about 6500 yr for a typical expansion velocity of 10 km s^{-1}. Dust-scattered light becomes undetectable due to sensitivity at a comparable radius for similar mass-loss rates, and the timescales probed are similar (e.g., Mauron & Huggins 2006; Mauron et al. 2013). Hence, both the progenitor mass and the total amount of mass ejected into the ISM, $M_{\rm ejecta}$ (which depends on the envelope's outer extent—e.g., $M_{\rm ejecta} \propto r_{\rm out}$, for a constant mass-loss rate at a constant expansion velocity), remain unknown. For example, in the case of IRC+10216, the best-studied mass-losing AGB star, the CSE seen in the above tracers extends to about 200″

$(3.5 \times 10^{17} \, \text{cm})$, and the inferred ejecta mass is only $M_{ejecta} \sim 0.15 \, M_\odot$, a small fraction of what this star has had to have lost, given its late evolutionary phase.

The unexpected discovery of a bow-shock structure and a turbulent wake extending over $2°$ ($\sim 4 \, \text{pc}$) in the sky, toward the AGB star, Mira, in a GALEX far-ultraviolet (FUV) image (Martin et al. 2007), resulted in a new method of probing the mass-loss history in AGB stars on very long timescales compared to the standard probes. Following the above discovery, very extended shock structures were also found around the carbon stars IRC+10216 and CIT 6 in GALEX FUV images by Sahai & Chronopoulos (2010) and Sahai & Mack-Crane (2014), who concluded that these structures result from the interaction of these stars' molecular winds with the ISM as they move through the latter. A far-infrared survey of a sample of 78 evolved stars (AGB stars and red supergiants), using the PACS instrument on board the Herschel Space Observatory, revealed bow shocks resulting from wind–ISM interactions in $\sim 40\%$ of the sample (Cox et al. 2012; some of the objects in this study had been known previously to show similar far-IR emission, e.g., R Hya, Ueta et al. 2006; αOri, Ueta et al. 2008 and Decin et al. 2012; R Cas, e.g., Ueta et al. 2010; and U Hya, Izumiura et al. 2011).

Surveys using all-sky archives have been used extensively to catalog and study bow shocks around massive stars (e.g., Brown & Bomans 2005; Peri et al. 2015; Kobulnicky et al. 2017). We are therefore carrying out a survey of GALEX images of a large sample of AGB stars, with the primary goals of searching for and characterizing extended circumstellar structures around these objects and using these to investigate their mass-loss history over unprecedented long timescales and its implications for their evolutionary status.

In this paper, we present first results from a survey of objects for which long-exposure GALEX images are available and have been examined so far. Future papers will focus on results from surveying the full GALEX archive of images. From our current survey, we have found ten objects with extended UV emission.[3] We do not discuss emission from the central stars in this paper. The plan of our paper is as follows. We first provide a summary of the archival data that we analyzed and the methodology used to search for the presence of extended UV emission associated with AGB stars (Section 2). In Section 3, we present our observational results for each object in which we found extended UV emission, together with the analysis used to characterize this emission. In Section 4, we quantitatively analyze the wind–ISM interaction and discuss the implications of our results for the mass-loss histories of these objects. In Section 5, we present a model spectrum of the FUV emission from an astrosphere assuming the current hypothesis for its origin, together with reference to an instrumental concept that can carry out the spectroscopic observations required to test this hypothesis. Finally, in Section 6, we present the main conclusions of our study.

2. Archival UV Observations

In our survey, we have first focused our attention on 92 AGB stars that lie in the fields of view (FOVs) of long-exposure ($>700 \, \text{s}$) FUV GALEX images (Morrissey et al. 2005), generally taken as part of the Medium Imaging Survey (MIS)

and various Guest Investigator Programs. The GALEX archive[4] contains FUV and near-UV (NUV) images with a bandpass (angular resolution) of 1344–1786 Å ($4{.}''5$) and 1771–2831 Å ($6{.}''0$), respectively, with a pixel size of $1{.}''5 \times 1{.}''5$ and an FOV of $1°.25$. A total of 92 such objects were found. The associated FUV and NUV images were downloaded from the archive, together with the associated GALEX point-source FUV and NUV catalogs for these fields.

2.1. Image Analysis

We followed a similar methodology as in Sahai & Mack-Crane (2014) to search for faint UV emission. First, all point sources listed in the UV point-source catalogs were removed using a customized IDL routine which replaces a small region covering each star's point-spread function with a tile of random noise representative of the surrounding sky. The sky noise was sampled separately at the four corners of each tile and linearly interpolated throughout, so as to preserve gradients in the local sky background to first order. In some situations the field stars are not properly removed; this can occur if there are many stars close together or if the star is very bright. In either case, a residue is left on the image. Two other artifacts that appear on the UV images are ghosts and hot spots. Both artifacts appear as doughnut shapes and can be clearly identified with the original image. After removing the point sources, the images are smoothed using IRAF's Gaussian smoothing function, "Gauss," with a FWHM of 5 pixels ($7{.}''5$), except for for U Ant, where we used 3 pixels ($4{.}''5$) as the emission is relatively bright.

Since the emission is relatively faint in most cases, and emission associated with interstellar "cirrus" is generally also present in the full circular FOV, we used the following criteria to identify UV emission associated with our targets.

1. There is extended UV emission all around the star that peaks in some part of a reasonably well-defined geometrical structure—the latter may be (a) circularly symmetric (ring), have either (b) a fan-shaped morphology or (c) a head–tail morphology, or be (d) a combination of (b) and (c).
2. There are extended regions of significantly lower-level (compared to the above) intensity around the above structure that can be identified as the general ISM.
3. For each source with noncircular emission morphology, we looked for a rough axis of symmetry for the structure, using the following strategy. The indicators we focused on were an increased brightness along part of the structure and a (roughly) diametrically opposed fainter tail. If the structure had a tail, we started our search directly across from the tail; for example, if the tail was aligned along, say, $PA = 0°$, we looked for a brightening along $PA = 180°$. If there was no easily identifiable tail structure, then we looked for a relatively brighter section on the periphery of the structure.

   We then made radial intensity cuts averaged over an azimuthal wedge with its apex centered on the star spanning a wide range in position angles around the symmetry axis. We generally used a fairly wide opening angle for the wedge, $\sim 80°$, in order to reduce sensitivity to local bright spots in the FUV emission since the FUV

Table 1
Observation Log

Name	Sp.Typ.	FUV Image Root[a]	FUV Exp.Time[b] (s)	NUV Image Root[c]	NUV Exp.Time[d] (s)
VX Eri	M3/4III	MISWZS03_27400_0183_0002	722.55	MISWZS03_27400_0183_0002	722.55
EY Hya	M7	MISDR1_24292_0467_0007	3352.05	MISDR1_24292_0467_0007	3352.05
R LMi	M6.5-9e	GI1_023004_HIP47886_0002	1605.1	GI1_023004_HIP47886_0001	3290.2
U Ant	C-N3	GI5_021008_U_Ant_0002	1119.05	GI5_021008_U_Ant_0001	6379.1
V Hya	C-N:6	GI1_023019_HIP53085_0001	2696.2	GI1_023019_HIP53085_0001	2696.2
RT Vir	M8III	GI5_021002_RT_Vir_0001	3473.85	GI5_021002_RT_Vir_0001	9079.9
R Hya	M6-9e	GI5_021003_R_Hya_0001	6029.75	GI5_021003_R_Hya_0001	7651.05
W Hya	M7.5-9e	GI5_021004_W_Hya_0001	4420.4	GI5_021004_W_Hya_0001	4420.4
RW Boo	M5III:	GI1_023006_HIP71802_0003	1721.	GI1_023006_HIP71802_0001	5113.0
RX Boo	M7.5-M8	GI5_021005_RX_Boo_0001	5161.45	GI5_021005_RX_Boo_0001	7657.65

Notes.
[a] OBJECT keyword in FUV Image fits file header.
[b] Total exposure time for FUV image.
[c] OBJECT keyword in NUV Image fits file header.
[d] Total exposure time for NUV image.

emission is quite faint and noisy. For each cut, we visually traced the intensity from large radii (where the cut intensity is equal to the average sky background intensity) to smaller radii and looked for a steep rise of the intensity expected in the region of interaction of the stellar with the ambient medium. We checked that this intensity rise is not sensitive to the opening angle of the azimuthal wedge by inspecting cuts with a range of opening angles ($\sim 40°$–$70°$).

The analysis of such radial intensity cuts for the astrospheres of IRC 10216 and CIT 6 shows that the termination shock is located at the peak of the intensity rise (R_1; Figure 3 in Sahai & Chronopoulos 2010), and the thickness of the astrosheath[5] is given by the distance between the peak and the radius at which the steeply falling intensity levels off (R_c; Figure 3 in Sahai & Chronopoulos 2010), either to a low-intensity plateau region that is brighter than the average sky background, or to the average sky background. The low-intensity plateau region likely represents emission from swept-up ISM material between the outer edge of the astropause and the bow-shock interface separating the shocked and unshocked ISM (R_2; Figure 3 in Sahai & Chronopoulos 2010).

Using the above methodology, we found extended FUV structures around ten stars. A log of the image fits files for these sources, together with the exposure times, are given in Table 1. We discuss these below in order of increasing R.A. One object, VX Eri, for which the association is tentative, is discussed at the end. In Table 2, we list specific published stellar properties: name (col. 1), Galactic coordinates (cols. 2–3), proper motion (col. 4; from GAIA DR3, Gaia Collaboration 2022),[6] mass-loss properties derived from CO data and modeling (mass-loss rate; col. 6), radial velocity (col. 7), wind expansion velocity (col. 8), the assumed CO-to-H_2 abundance ratio (col. 9), and adopted distance for the mass-loss estimation (col. 5). We also list observed properties of the extended FUV emission related to the wind–ISM interaction, which include an estimate of the average FUV intensity in the interaction region (col. 11), the

termination shock radius (R_1) and the outer radius of the astropause (R_c) extracted from the radial intensity cuts (cols. 12–13), and characteristics of the emission morphology (col. 15). Conservative estimates of the errors are (i) R_1: $\lesssim 5\%$, when a sharp peak is seen at the termination shock (otherwise the error is typically $\lesssim 10\%$), (ii) R_c: $\lesssim 10\%$, and (iii) R_2: $\lesssim 15\%$.

For VX Eri, no published CO data could be found; hence, we have used its IRAS 60 μm flux (0.62 Jy) to derive a rough estimate of the dust-mass loss rate, $\dot{M}(d)$, using the methodology given by Jura (1986). The bolometric flux, $F = 1.55 \times 10^{-7}$ erg cm^{-2} s^{-1}, and the mean wavelength for emission, $\lambda_e = 1.7 \mu$m required for this method, were estimated from the spectral-energy distribution, extracted using the VizieR Photometry viewer[7] over the 0.35–60 μm range. The gas mass-loss rate was derived from $\dot{M}(d)$, assuming a typical gas-to-dust ratio of 200; we also assume a typical circumstellar expansion velocity of 10 km s^{-1} for this object.

3. Results

3.1. EY Hya

The FUV image of EY Hya (Figure 1) shows a head–tail structure around the star. This structure has no counterpart in the NUV image. The long axis of this structure is closely aligned with EY Hya's proper motion vector.[8] We therefore infer that the western periphery of the head represents the termination shock of the astrosphere around EY Hya. The tail appears to consist of two long filamentary stuctures—T1 (length $\sim 340''$) and T2 (length $\sim 520''$). The extended structure at $250''$ between PA = $25°$ and PA = $40°$ (Region A in Figure 1) is not associated with EY Hya but is due to an imperfectly subtracted, very bright point source located at an offset of $275''$ (at PA = $25°$) from EY Hya, which left some residual brightness after being removed.

A radial intensity cut averaged over an azimuthal wedge with its apex centered on the star and spanning the range from PA = $-60°$ to $-140°$ (Figure 2) shows a peak at radius $r = 130''$, with a rapid decline of the intensity for larger radii

---

[5] See Figure 2(d) in Ueta (2008) for a definition of the terms termination shock, astrosheath, astropause, and bow shock used to describe an astrosphere.
[6] With the exception of W Hya, where we provide the Hipparcos value from van Leeuwen (2007) since it is not listed in GAIA DR3.

[7] http://vizier.cds.unistra.fr/vizier/sed/
[8] The proper motion for each source has been corrected for solar motion, see Section 4.2.1; the corrected values are used in all further reference to this parameter.

Table 2
Stellar, Mass-loss, and Measured Astrosphere Parameters

Name	Long. (deg)	Lat. (deg)	PM (mas yr^{-1})	D_0 (kpc)	$\dot{M}_{w,0}$ ($10^{-6}\,M_\odot$ yr^{-1})	V_{lsr} (km s^{-1})	V_e (km s^{-1})	$f(CO)_0$ (10^{-3})	References	Aver.Int. (10^{-4} cps pix^{-1})	R_1 ($''$)	R_c ($''$)	$(R_c - R_1)/R_1$	Morph.
(1)[a]	(2)	(3)	(4)	(5)	(6)	(7)	(8)	(9)	(10)	(11)	(12)	(13)	(14)	(15)
VX Eri	198.3011	−51.1339	14.79	0.657	0.023	−21.9	10	0.3	1	1.8	290.0	460.0	0.59	w-ISM+w-w?
EY Hya	225.3952	26.1423	11.55	0.300	0.25	22.5	11	0.2	2	0.84	130.0	170.0	0.31	w-ISM+bs
R LMi	190.5954	49.7711	2.398	0.330	0.26	0	7.5	0.3	3	0.34	295.0	375.0	0.27	w-ISM
U Ant	276.2241	16.1419	31.61	0.260	10	24.5	19	1.0	4	4.3	175.0	255.0	0.46	w-ISM+bs+w-w?
V Hya	268.9649	33.6014	16.31	0.380	2.5[b]	−17.4	15, 45, 200[b]	1.0	7	0.44	365[c]	430[c]	0.18[c]	(see text, Section 3.4)
RT Vir	310.3571	67.8959	41.05	0.136	0.5	17.4	7.8	0.2	2	0.57	65.0	95.0	0.46	w-ISM+bs
R Hya	314.2230	38.7498	55.48	0.118	0.16	−10	12.5	0.2	5	0.73	120.0	145.0	0.21	w-ISM
W Hya	318.0224	32.8108	79.01	0.104	0.078	41	8.5	0.2	5	1.1	220.0	290.0	0.32	w-ISM+w-w
RW Boo	50.0855	65.7340	15.61	0.307	0.044	5[d]	17.3	0.3	6	0.39	260.0	310.0	0.19	w-ISM+bs?
RX Boo	34.2774	69.2127	52.52	0.128	0.0649	2	11.2	0.3	6	0.66	325.0	475.0	0.46	w-ISM

Notes.

[a] Column headings: (1) Name, (2) Galactic Longitude, (3) Galactic Latitude, (4) Proper Motion, (5) Distance to Star, (6) Mass-loss Rate, (7) Stellar Velocity, relative to the LSR, (8) Wind Expansion Velocity, (9) CO-to-H_2 abundance ratio, (10) Reference for cols. 4–6, (11) Average FUV Intensity of Termination Shock (10^{-4} counts per second (cps) pix^{-1} = 0.622×10^{-19} erg s^{-1} cm^{-2} Å^{-1} arcsec^{-2}), (12) Termination Shock Radius (angular) from Radial Intensity Cut, (13) Astropause Radius (angular) from Radial Intensity Cut, (14) Astrosheath Fractional Width, and (15) Morphology of Extended FUV Emission—w–ISM (wind–ISM interaction), bs (emission from shocked ISM), w–w (wind–wind interaction).

[b] The mass outflow from V Hya is complex with multiple components; the mass-loss rate value is the sum of the mass-loss rates for the three components with different expansion velocities (listed in Col. 7) as identified by Knapp et al. (1997).

[c] These values apply to the westernmost part of the elliptical ring centered to the west of the star, extracted from a radial intensity cut spanning a narrow azimuthal wedge around the ring's minor axis.

[d] The value of V_{lsr} has been inferred from the CO J = 1–0 and 2–1 line spectra in Díaz-Luis et al. (2019) since the tabulated value in this reference (−4.99 km s^{-1}) appears to have an incorrect sign.

References: (1) this study, (2) Olofsson et al. (2002), (3) Danilovich et al. (2015), (4) Kerschbaum et al. (2017), (5) De Beck et al. (2010), (6) Díaz-Luis et al. (2019), (7) Knapp et al. (1997).
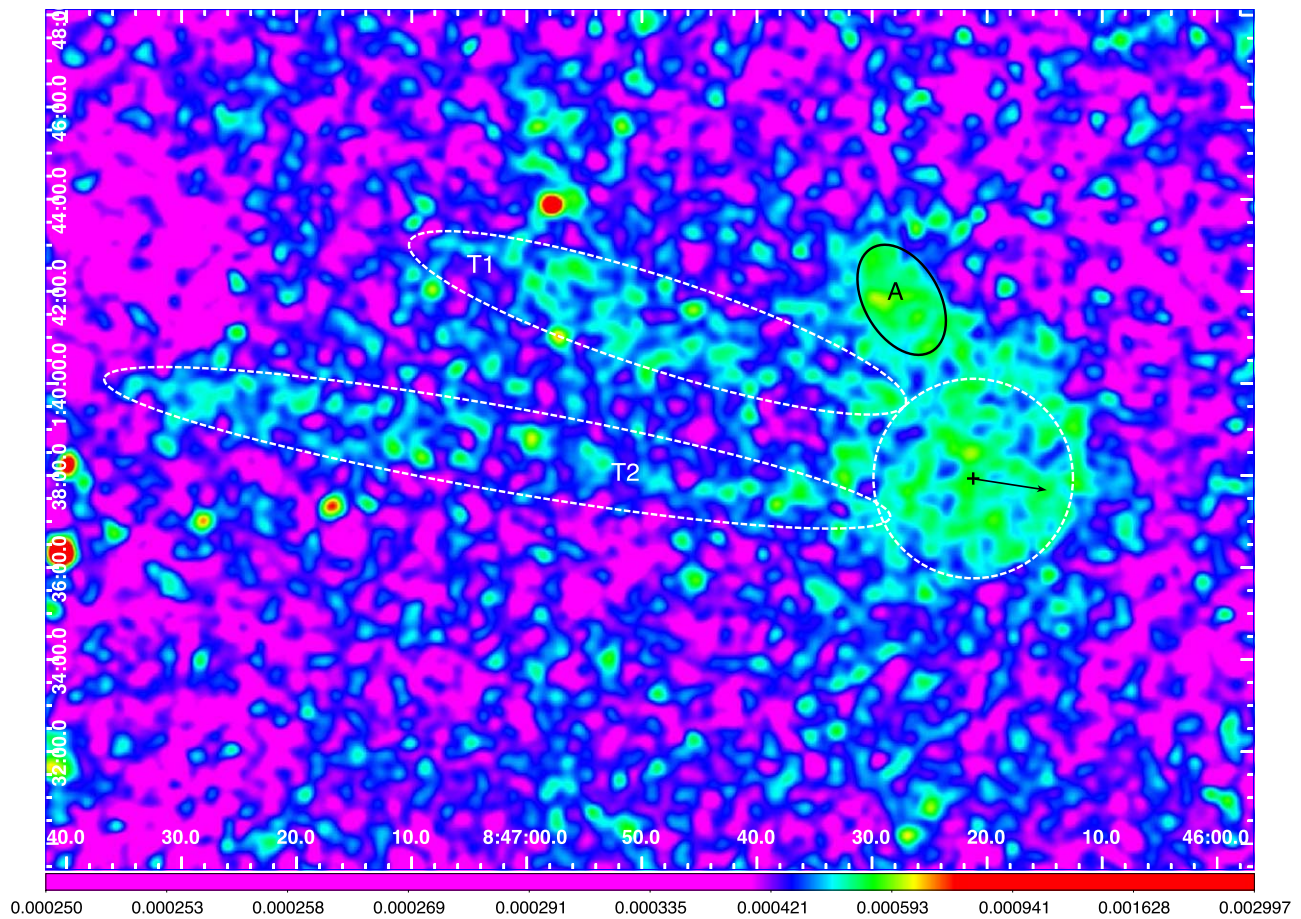
Figure 1. The FUV emission toward EY Hya, imaged with GALEX. The large white dashed circle, with radius of 130″, delineates the radial extent of the termination shock in the astrosphere, west of EY Hya. Two long filamentary structures that comprise the tail region of the astrosphere are labeled T1 and T2. The emission in region labeled A is due to an imperfectly subtracted, very bright point source located at an offset of 275″ (at PA = 25°) from EY Hya. The black cross shows the star's location. Vector shows the star's proper motion of 9.5 mas yr^{-1} at PA = 261°, magnified by a factor of 10^4. North is up and east is to the left. The scale bar shows intensity in cps pix^{-1}.
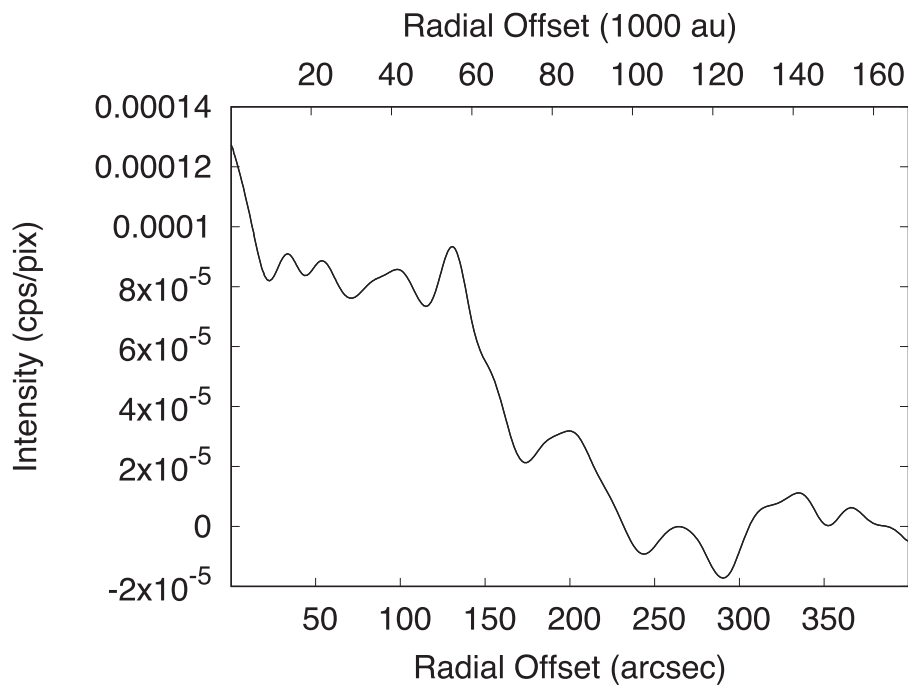

Figure 2. Radial intensity cut of the FUV emission around EY Hya, averaged over an azimuthal wedge with its apex centered on the star and spanning the range from PA = −60° to −140°. The average surrounding sky intensity has been subtracted from the cut.
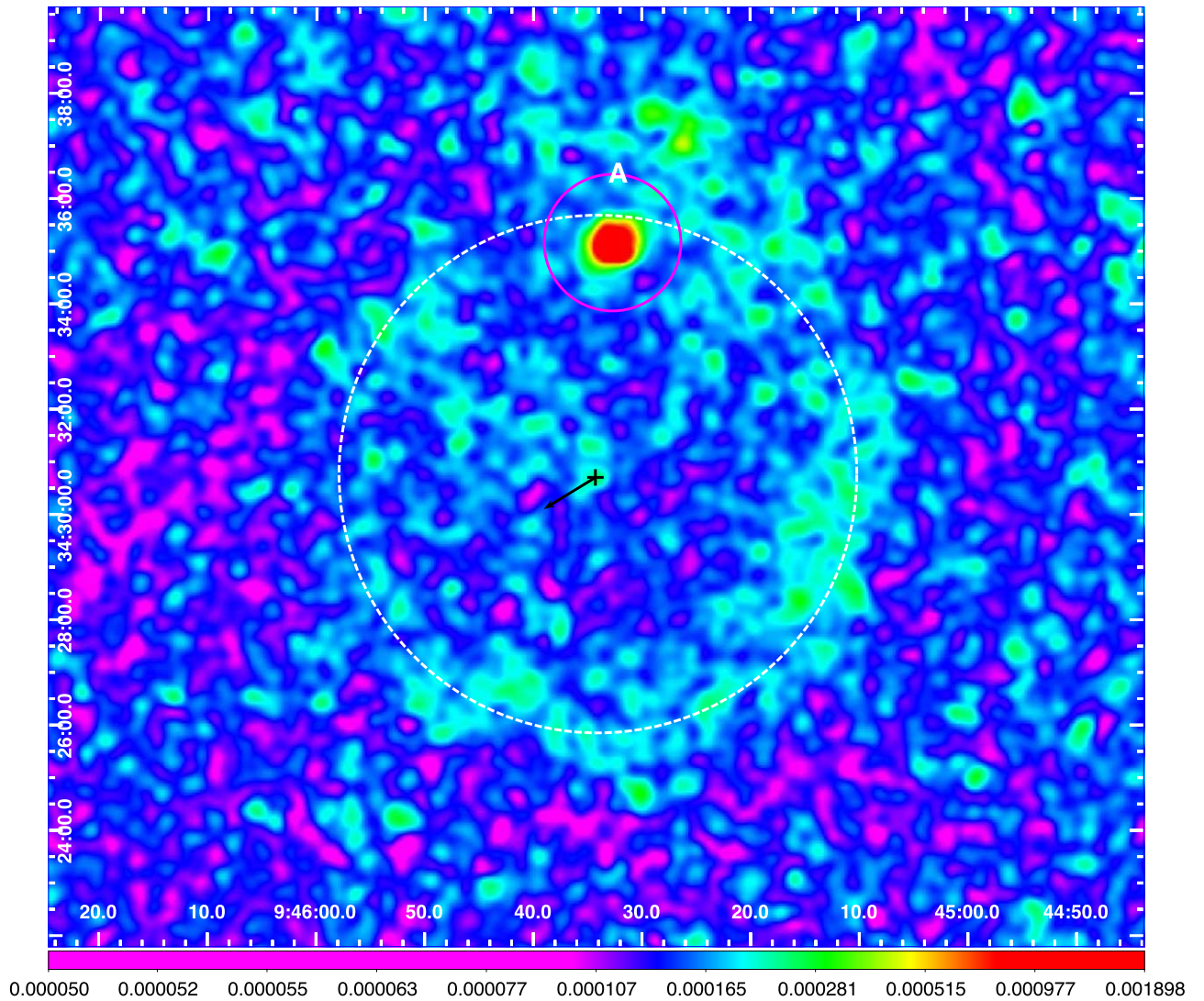
Figure 3. The FUV emission toward R LMi, imaged with GALEX. The large white dashed circle, with radius of 295″, delineates the radial extent of the termination shock in the astrosphere; black cross shows location of the star. Vector shows the star's proper motion of 6.9 mas yr^{-1} at PA = 122°, magnified by a factor of 10^4. Region A (magenta circle) shows local environment around two point sources that could not be removed. North is up and east is to the left. The scale bar shows intensity in cps pix^{-1}.

out to $r \sim 170''$. This is followed by a region of lower FUV intensity, out to $r \sim 230''$ where its brightness becomes comparable to the surrounding sky intensity. We infer a termination-shock radius of $R_1 = 130''$ and an outer radius of the astropause, $R_c \sim 230''$. The low-intensity region in the range $r \sim 170''–230''$ likely represents emission from swept-up ISM material between the outer edge of the astropause and the bow-shock interface separating the shocked and unshocked ISM.

3.2. R LMi

The FUV image of R LMi (Figure 3) shows a partial ringlike structure around the star. This extended FUV emission structure has no counterpart in the NUV image. A minor segment of the ring structure is overlapped by two bright point sources within the circle labeled A in the images that could not be removed. The ring structure is somewhat brighter overall in a semicircular azimuthal wedge around PA $\sim -120°$. A radial intensity cut averaged over an azimuthal wedge with its apex centered on the star and spanning a 320° azimuthal range around PA = 120° (Figure 4) shows a broad, flat-topped peak

at radius $r = 295''$, with a full-width at half-maximum of $\sim 90''$. The intensity declines rapidly beyond radius $r \gtrsim 320''$, reaching the brightness level of the surrounding sky intensity at $r \gtrsim 375''$. It is not clear exactly where the termination shock resides within the broad intensity hump; as a compromise we assume that it resides in the middle, at $R_1 = 295''$; the outer radius of the astropause lies at $R_c \sim 375''$. The proper motion of this star is relatively small (2.4 mas yr^{-1}), consistent with the roughly circular shape of its astrosphere.

3.3. U Ant

The FUV image of U Ant (Figure 5) shows a ringlike structure around the star. This extended FUV emission structure has no counterpart in the NUV image. The FUV ring is much larger than the ringlike structure observed in the radial intensity cuts of Herschel/PACS images at a radius of 42″ (Kerschbaum et al. 2010; Cox et al. 2012). Although the FUV emission can be seen all around the star, it is significantly brighter between position angles of $\sim -160°$ to $\sim -40°$, encompassing the direction of the star's proper motion. We
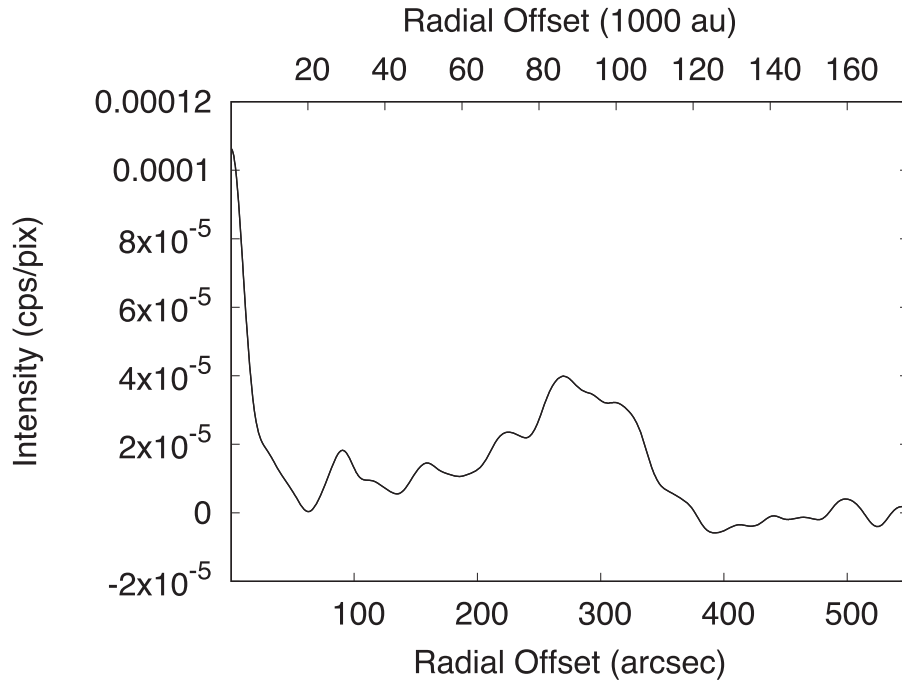
Figure 4. Radial intensity cut of the FUV emission around R LMi, averaged over an azimuthal wedge with its apex centered on the star and spanning a 320° angular range around PA = 120°. The average surrounding sky intensity has been subtracted from the cut.

infer that this bright region represents the termination shock of the astrosphere resulting from the interaction of the star's wind with the ISM, and its symmetry axis is oriented at PA $\sim -100°$. However, we note the possible presence of a very faint tail in the FUV emission that extends toward the southwest direction, suggesting that the symmetry axis of the astrosphere is at PA $\sim -45°$. A radial intensity cut averaged over an azimuthal wedge with its apex centered on the star, spanning the range from PA $= -60°$ to $-140°$ (Figure 6), shows a prominent peak at radius $r = 175''$, with a rapid decline of the intensity for larger radii out to $r \sim 255''$. This is followed by a shallow decline in a region of low FUV intensity, out to $r \sim 420''$, where its brightness becomes comparable to the surrounding sky intensity. We infer a termination-shock radius of $R_1 = 175''$ and an outer radius of the astropause, $R_c \sim 255''$. The low-intensity region in the range $r \sim 255''$–$420''$ likely represents emission from swept-up ISM material between the outer edge of the astropause and the bow-shock interface separating the shocked and unshocked ISM.

A secondary, weaker peak is seen in FUV intensity cut at $r = 105''$—the PACS 160 μm imaging of U Ant shows faint, patchy emission beyond $42''$ ring but lack the sensitivity to reveal a counterpart to the FUV peak. Since this peak lies interior to the termination shock, we suggest that it is the result of a wind–wind interaction similar to the one that has been postulated for the $42''$ ring.

Izumiura et al. (1997) found, using IRAS 60 and 100 μm imaging, two extended dust shell structures in U Ant; they used these data to construct a double-shell model of this source. Their inner shell with a median radius of $51''$ likely corresponds to the shell seen in the PACS images; their outer shell, which is separated from the inner one by $150''$ likely corresponds to the astrosphere directly revealed in the FUV images.

3.4. V Hya

The FUV image of V Hya is complex, with a central elongated feature oriented east–west, and two large, roughly elliptical ringlike structures (Figure 7). These structures have no counterpart in the NUV image. The central elongated structure may be associated with the interacting of the extended extreme-velocity highly collimated blobby outflows seen both in CO millimeter-line emission (Sahai et al. 2022) as well as optical line emission (Sahai et al. 2016; Scibelli et al. 2019) with the ambient circumstellar medium.

The centers of the FUV emission rings lie along a roughly east–west axis. The ratio of major-to-minor axis of the rings is $\sim$1.45—assuming these are intrinsically circular, we conclude that their axis is inclined by $\sim$45° to the sky plane. A similar orientation has been found for the axes of the rings seen in the disk around V Hya via CO millimeter-line imaging (Sahai et al. 2022). The FUV rings may be associated with the large high-velocity bipolar parabolic outflows seen in V Hya via CO millimeter-line imaging, whose axes are also aligned roughly east–west (Sahai et al. 2022). In this scenario, the FUV emission would result from molecular H_2 interaction with the ISM or the circumstellar medium resulting from a spherical, slowly expanding wind from V Hya. Some excess FUV emission (over the average sky background) is seen near the transverse structure labeled T.

The major axes of the FUV elliptical ring structures is about $750''$, roughly a factor of 35 larger than the widest extent of these outflows as seen in CO emission ($\sim$20''), showing that these outflows have been operating for a much longer timescale (t_{out}(FUV)) than could be estimated from the CO data (t_{out}(CO)). A rough estimate of t_{out}(CO) can be made from dividing the radial distance between the star and the tip of the outflow seen in Figure 13(d) of Sahai et al. (2022; $16'' \times 311$ pc/cos $i = 7035$ au), where $i \sim 45°$ is the inclination angle of the outflow axis to the sky plane, by an estimate of the
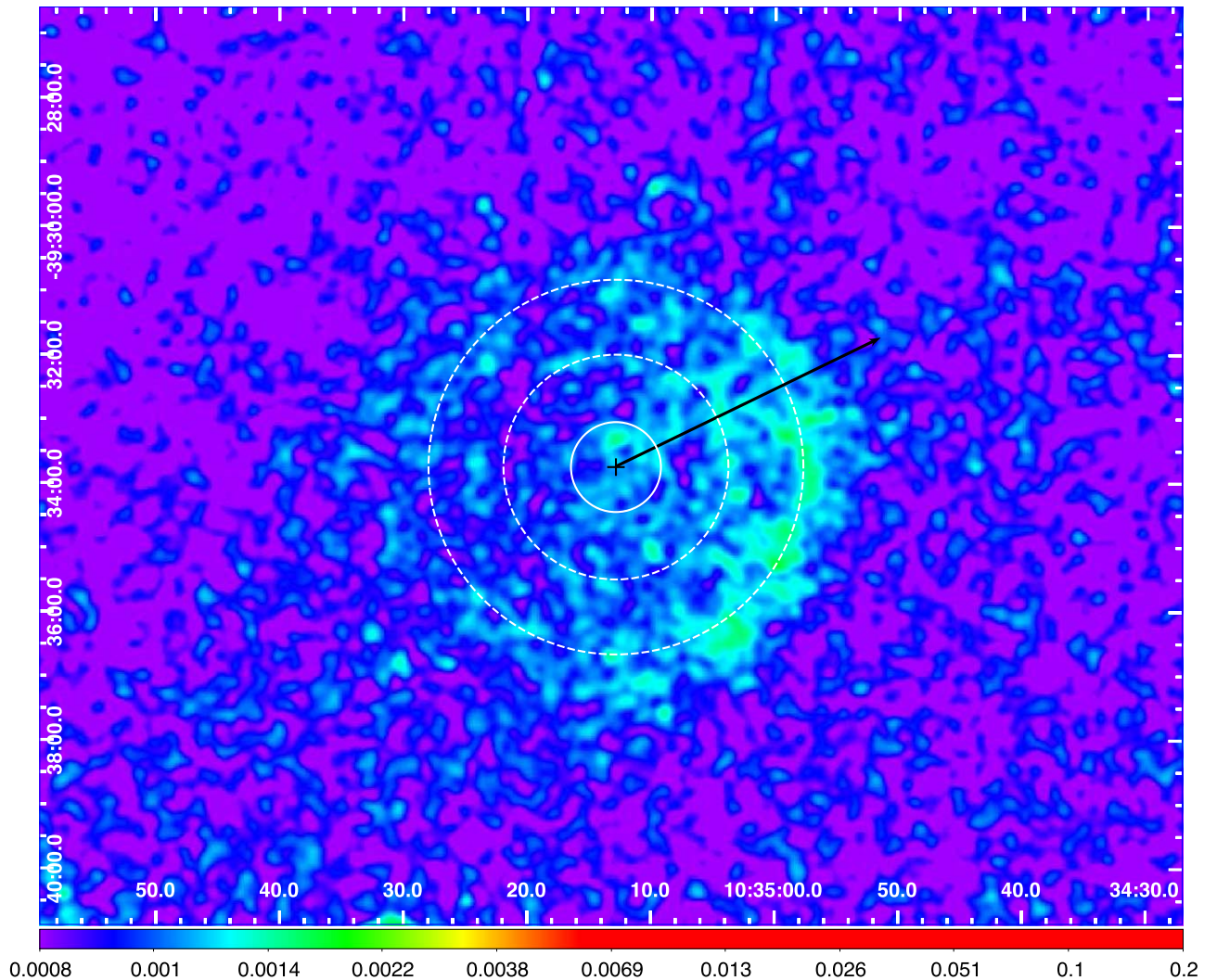
Figure 5. The FUV emission toward U Ant, imaged with GALEX. The large white dashed circle, with radius of 175″, is a fit to the estimated radial location of the termination shock in the astrosphere, seen to the west of U Ant. The smaller dashed circle, with radius of 105″, marks the location of an intensity peak in the radial intensity cut in Figure 6. The small white dashed circle, with radius of (42″) shows the location of the detached shell seen in the far-IR by Cox et al. (2012). All circles are centered on the star's location (black cross). Vector shows the star's proper motion of 27.5 mas yr^{-1} at PA = 296°, magnified by a factor of 10^4. North is up and east is to the left. The scale bar shows intensity in cps pix^{-1}.

expansion velocity of the material there, V_{out}, assuming radial expansion. Correcting for projection, the radial velocity offset of the CO emission seen in Figure 13(d) of Sahai et al. (2022) at 47 km s^{-1} from the systemic velocity (-17.4 km s^{-1}) of 64.4 km s^{-1} implies a 3D expansion velocity of $\sim$185 km s^{-1}, which results in an expansion age of t_{out}(CO) $\sim$ 180 yr. Assuming the same expansion velocity for the material seen in the FUV elliptical ring but located at a projected radial distance that is about a factor of 25 larger than that seen in CO, we find an expansion age of t_{out}(FUV) $\gtrsim$ 4500 yr. This age is a lower limit because the material seen in the FUV emission must have slowed down due to its interaction with the ambient medium.

Because the FUV rings have elliptical shapes, the use of a large angular wedge for a radial intensity cut significantly dilutes the intensity peak produced by the rings. Hence we have made a 20°-wide cut around PA = $-90°$ to estimate the radius of the western outflow's interaction with the ISM. The cut (Figure 8) shows a peak at $r \sim 365″$ that corresponds to the westernmost part of the elliptical ring centered west of the star (dashed black ring in Figure 7), along its minor axis. A less

prominent hump is seen at $r \sim 135″$ that corresponds to the westernmost part of the elliptical ring centered east of the star (dashed-dotted white ring in Figure 7).

There is no obvious indication of the interaction of a spherical wind with the ISM.

3.5. RT Vir

The FUV image of RT Vir shows an elongated head−tail structure, with a bow shock−like shape east of the star and an extended tail to its west. This extended FUV emission structure has no counterpart in the NUV image. The long axis of this structure is aligned along PA $\sim$ 192°, i.e., very close to that of the proper-motion vector (Figure 9). We therefore infer that this structure represents the termination shock of the astrosphere around RT Vir. A radial intensity cut averaged over an azimuthal wedge with its apex centered on the star and spanning the range from PA = 65° to 145° (Figure 10) shows a peak at radius $r = 65″$, with a fast decline of the intensity for larger radii out to $r \sim 95″$. This is followed by a shallower decline in a region of low FUV intensity, out to $r \gtrsim 240″$,
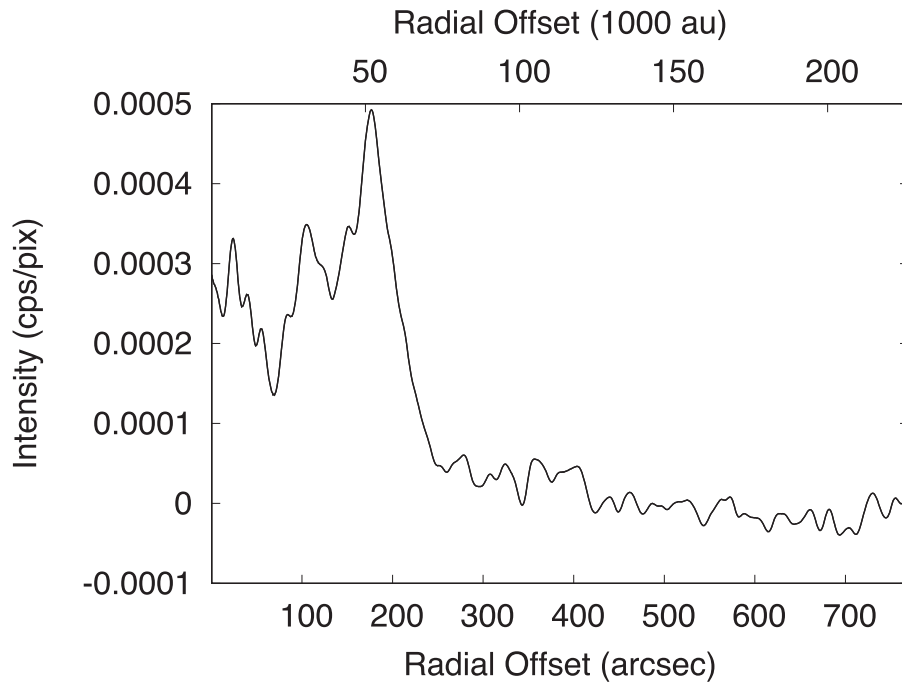
Figure 6. Radial intensity cut of the FUV emission around U Ant, averaged over an azimuthal wedge with its apex centered on the star and spanning the range from PA = −60° to −140°. The average surrounding sky intensity has been subtracted from the cut.
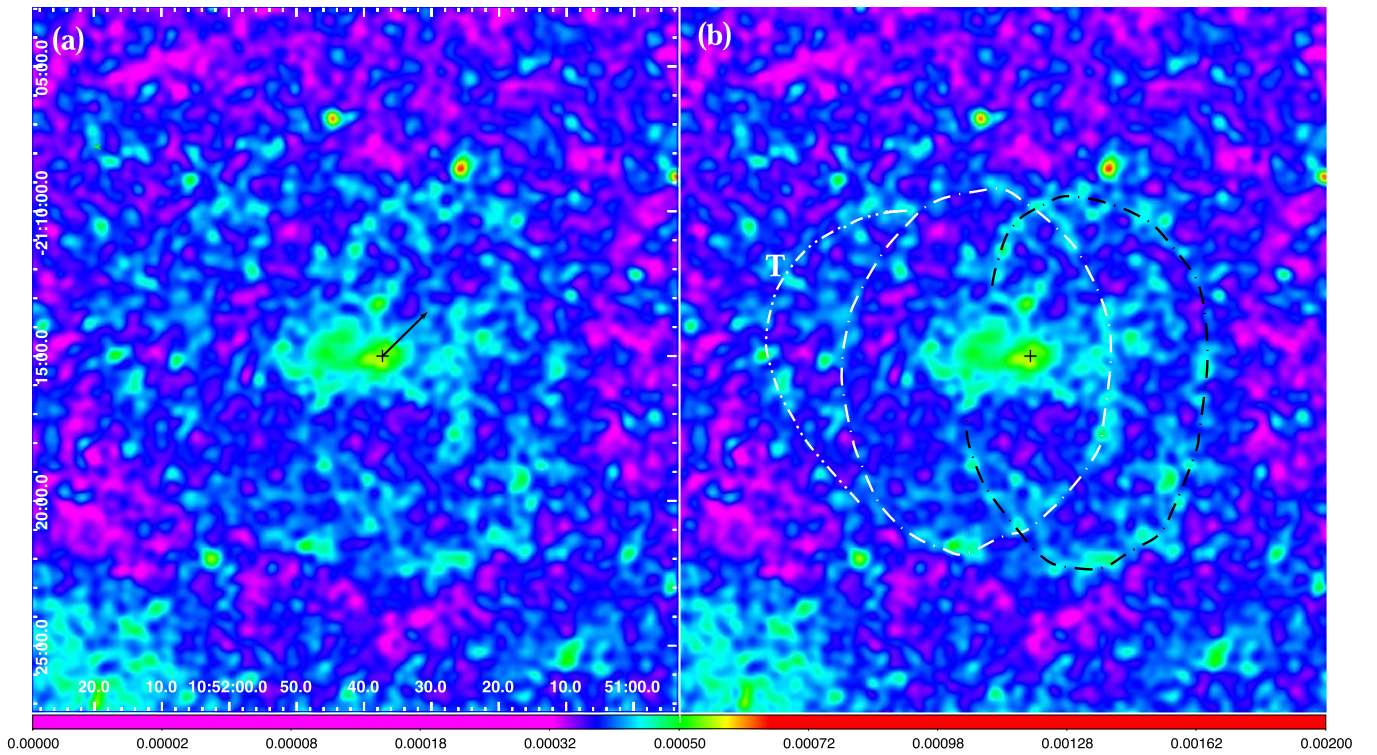

Figure 7. The FUV emission toward V Hya, imaged with GALEX. In panel (a) black cross shows the location of the star, and vector shows the star's proper motion of 12.9 mas yr^{-1} at PA = 315°, magnified by a factor of 10^4. In panel (b), dashed-dotted white elliptical arcs (dashed black elliptical arc) delineate extended regions of FUV emission that are likely associated with the blueshifted (redshifted) large parabolic outflows seen in CO emission by Sahai et al. (2022). Excess FUV emission (over the average sky background) is seen near the transverse structure labeled T. North is up and east is to the left. The scalebar shows intensity in cps pix^{-1}.

where its brightness becomes comparable to the surrounding sky intensity. We infer a termination-shock radius of $R_1 = 65''$ and an outer radius of the astropause, $R_c \sim 95''$. The low-intensity region in the range $r \sim 95''$–$240''$ likely represents emission from swept-up ISM material between the outer edge

of the astropause and the bow-shock interface separating the shocked and unshocked ISM.

There is a locally bright extended structure near the end of the tail (region A in Figure 9) that may or may not belong to the astrosphere.
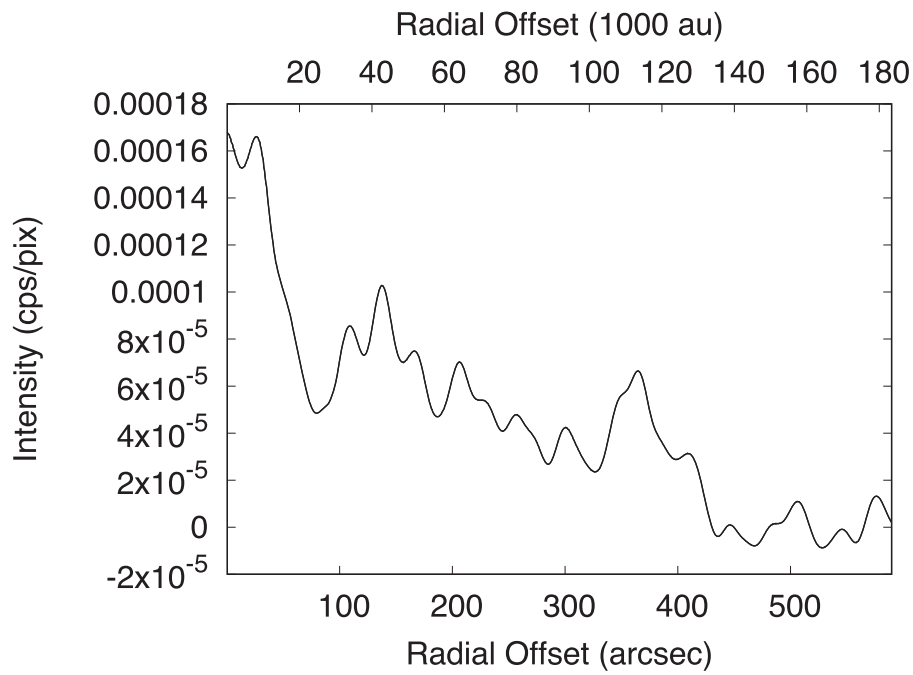
Figure 8. Radial intensity cut of the FUV emission around V Hya, averaged over an azimuthal wedge with its apex centered on the star and spanning the range from PA = −100° to −80°. The average surrounding sky intensity has been subtracted from the cut.
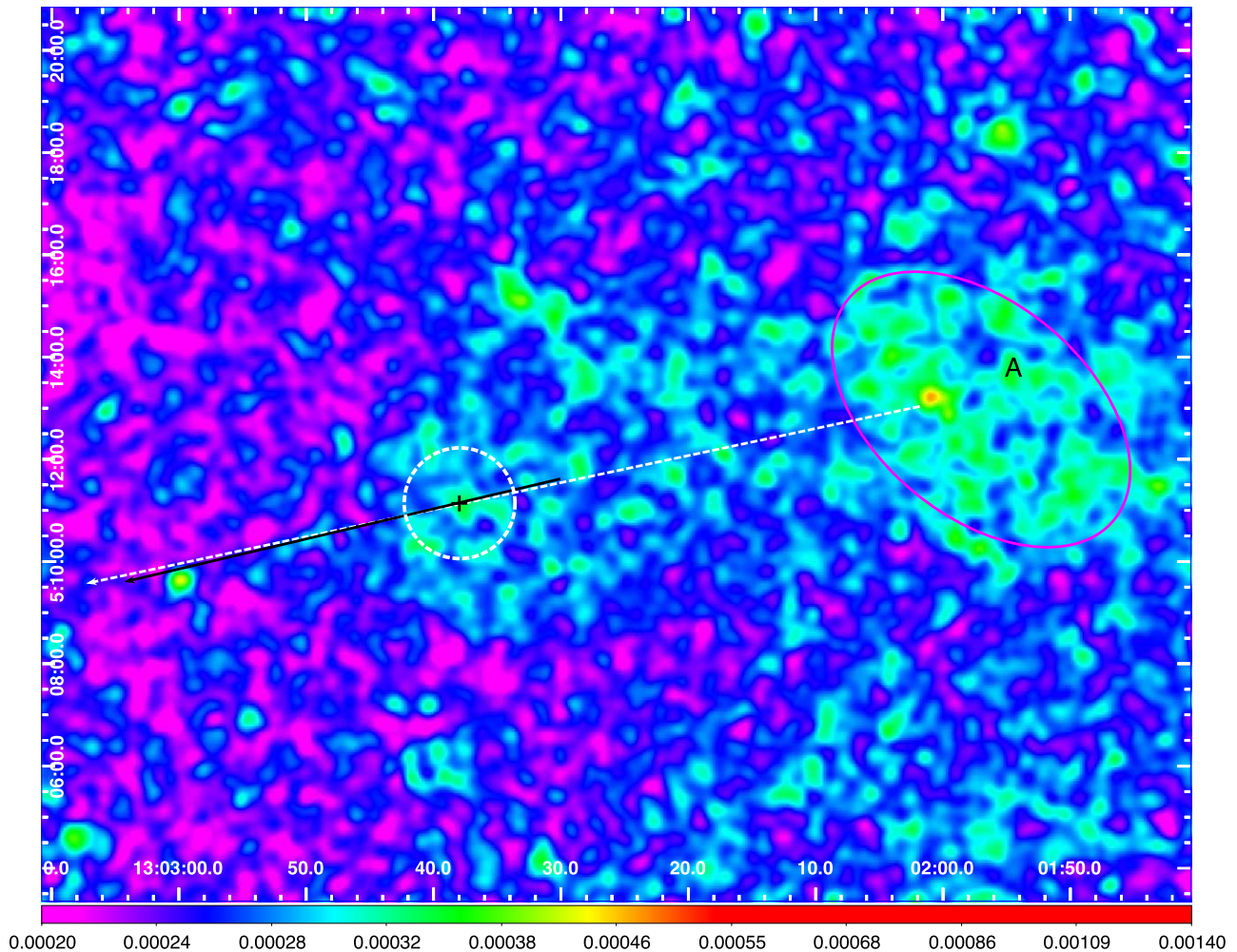

Figure 9. The FUV emission toward RT Vir, imaged with GALEX. The white dashed circle, with radius of 65″, delineates the termination shock in the astrosphere, east of the star (black cross). Vector shows the star's proper motion of 52.6 mas yr^{-1} at PA = 103°, magnified by a factor of 10^4. Region A (magenta ellipse) shows a locally bright region near the end of the astrosphere tail. North is up and east is to the left. The scale bar shows intensity in cps pix^{-1}.
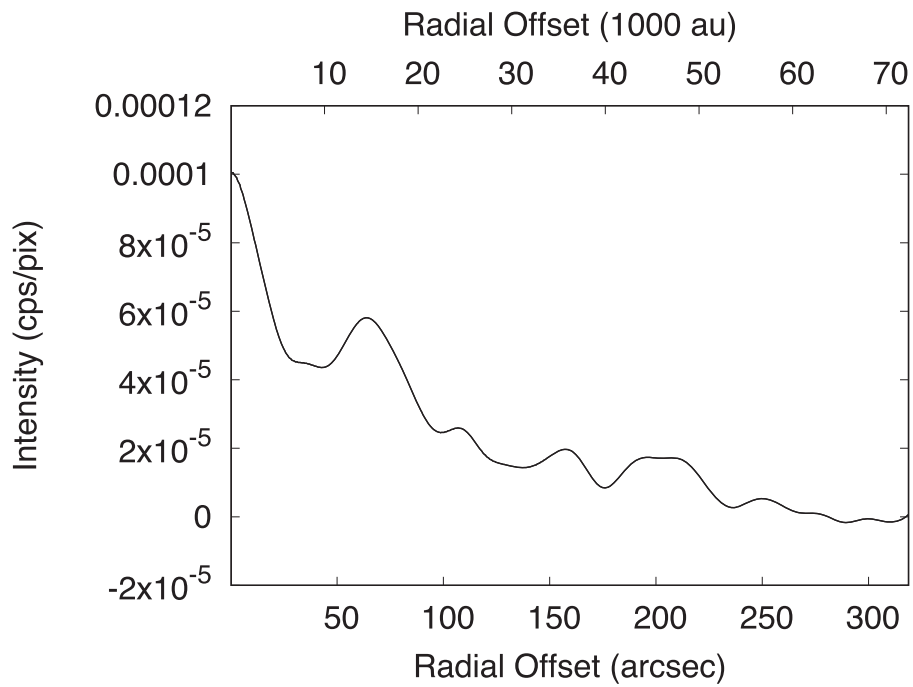
Figure 10. Radial intensity cut of the FUV emission around RT Vir, averaged over an azimuthal wedge with its apex centered on the star and spanning the range from PA = 65° to 145°. The average surrounding sky intensity has been subtracted from the cut.
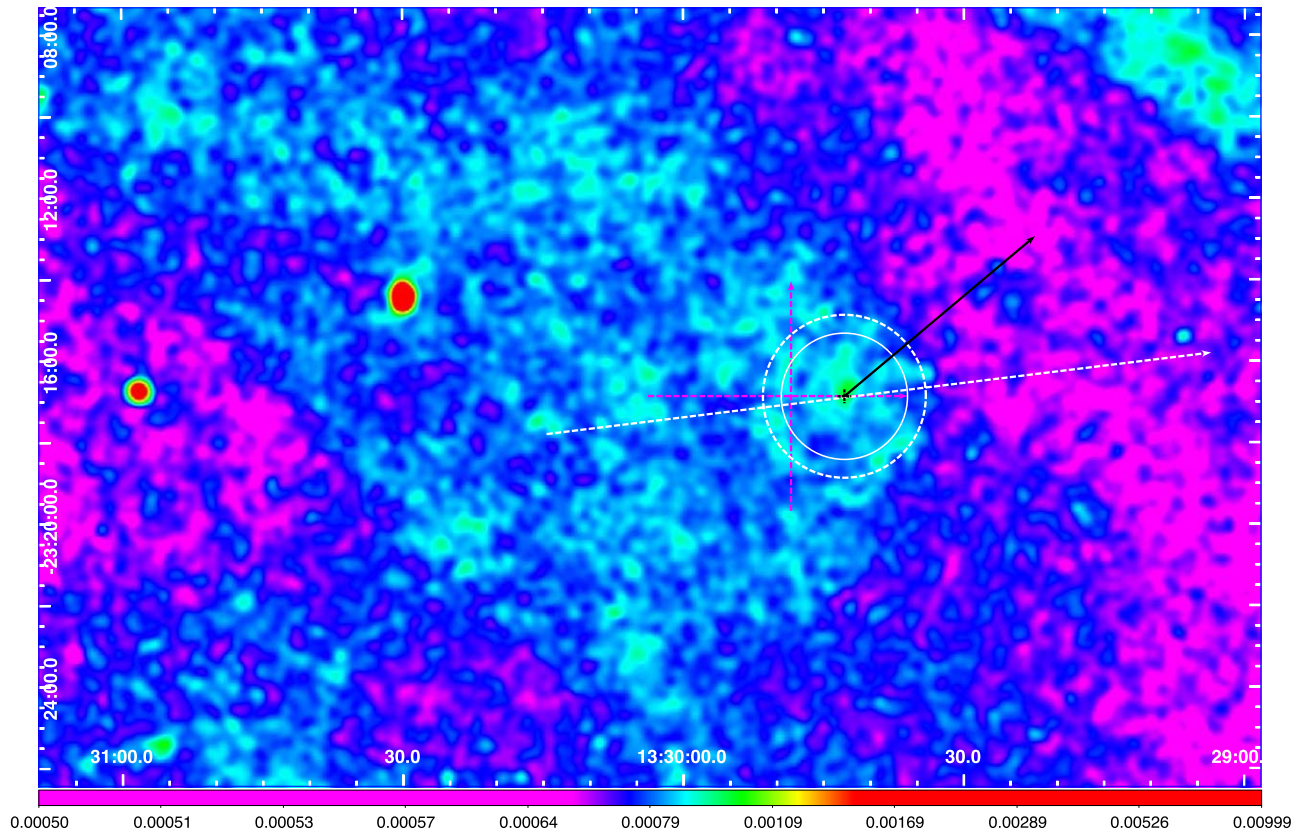
Figure 11. The FUV emission toward R Hya, imaged with GALEX. The white dashed circle, with radius of 120″, delineates the radial extent of the termination shock in the astrosphere, west of R Hya (black cross); white solid circle delineates a termination-shock radius of 93″ estimated from far-IR imaging by Cox et al. (2012). Black vector shows the star's proper motion of 36.7 mas yr^{-1} at PA = 310°, magnified by a factor of 10^4; white vector shows symmetry axis of the fan-shaped astrosphere. North is up and east is to the left. The scale bar shows intensity in cps pix^{-1}.

Figure 12. Radial intensity cut of the FUV emission around R Hya, averaged over an azimuthal wedge with its apex centered on the star and spanning the range from PA = −123° to −43°. The average surrounding sky intensity has been subtracted from the cut.
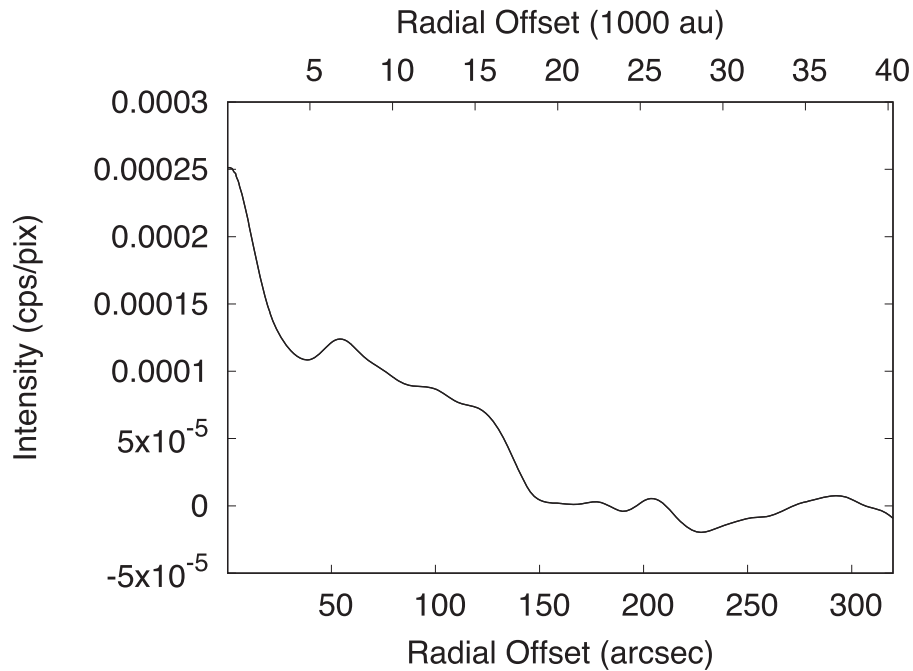
3.6. R Hya

The FUV image of R Hya shows an elongated fan-shaped structure, with a bow shock−like shape to the west of the star (Figure 11). This extended FUV emission structure has no counterpart in the NUV image. The symmetry axis of this structure is aligned along PA ∼ −82°, i.e., within 32° of the proper-motion vector; we infer that this structure represents the astrosphere around this star. A similar wide fan-shaped structure has been seen in the far-infrared at 70 μm with Spitzer (Ueta et al. 2006) and at 70 and 160 μm with PACS (Cox et al. 2012) but appears to be much more limited in extent compared to the FUV fan structure. The maximum north–south (east–west) extent of the fan structure as seen in the PACS 70 μm image is ∼340″ (∼385″), as denoted by dashed vertical (horizontal) magenta vectors in Figure 11—these vectors lie well within the FUV emission structure. Cox et al. (2012) derive a termination-shock radius of 93″ from their far-IR imaging.

A radial intensity cut of the FUV emission around R Hya, averaged over an azimuthal wedge (spanning the range from PA = −123° to −43°) with its apex centered on the star (Figure 12), show a steep decline in the intensity starting at $r \gtrsim 120″$ and reaching the background sky level at $r \sim 145″$. We infer that the termination-shock radius is $R_1 = 120″$, which is larger than the value derived from the far-IR data. Narrowing the opening angle of the azimuthal wedge to 40° makes no significant difference to the radial intensity distribution. We do not find any indication of a dramatic change in the radial FUV intensity at ∼93″. We infer an outer radius of the astropause, $R_c \sim 145″$.

3.7. W Hya

The FUV image of W Hya shows an overall head−tail morphology but with an amazingly extensive and complex structure (Figure 13), which includes both azimuthal and radial features. The NUV image of W Hya does not show these structures. Among the azimuthal features, there are partial ringlike structures that produce noticeable intensity peaks in a radial intensity cut, averaged over an azimuthal wedge with its apex centered on the star, covering the azimuthal range PA = 95° to 235° (this range is selected to be as wide as possible but still avoid bright radial features; Figure 14). A strong, sharp intensity peak at $r = 65″$ is due to the presence of a ring of the same radius, also seen in a 70 μm PACS images (Cox et al. 2012). This is followed by a weaker but sharp intensity peak at $r = 160″$ and a broader, asymmetric peak with its centroid at $r \sim 220″$. There are counterparts to each of these peaks in the 160 μm PACS radial intensity cuts; Cox et al. (2012) list only the outer one (at $r \sim 230″$) in their study. These intensity peaks correspond to partial ringlike structures in the FUV image. There are several large azimuthal structures at larger radial distances (marked T_1–T_3).

Numerous radial features (both close to and far away from star) are also seen in the FUV image—some of these may represent collimated outflows. These are labeled as A, B, ... G. Features A, B, and C show diametrically opposed pairs (denoted with subscripts 1 and 2, e.g., A_1 and A_2), i.e., and may be bipolar outflows. The tail region extends toward the north-northwest (features F and G). We find radial features in the PACS 70 and 160 μm images of W Hya from the Cox et al. (2012) study, located at position angles similar to those of outflows A_1, A_2, (B_2+D), (C_1+B_1), and (F+G).[9] Cox et al. (2012) mention only the counterpart to the A_1 outflow (as a jetlike extension pointing roughly northeast) but not the other radial features.

---

[9] We have grouped together the FUV outflows that appear as one azimuthally broad feature in the far-IR. Features F+G cannot be distinguished from the bright FUV emission in the near vicinity of the star, but we find an azimuthally broad far-IR feature in this region that roughly spans the azimuthal range covered by F and G.
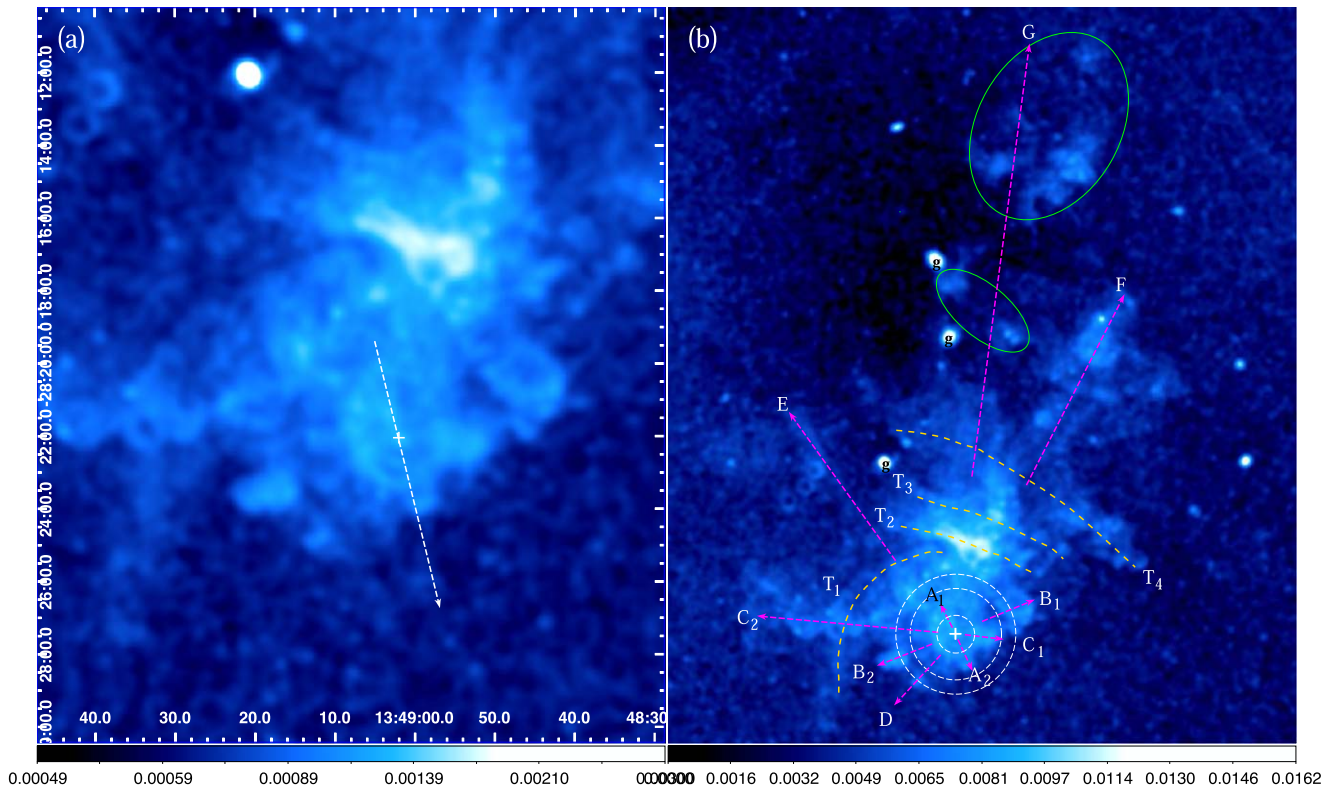
Figure 13. The FUV emission toward W Hya (white cross), imaged with GALEX. (a) The FUV emission in the near vicinity of W Hya (white cross); white dashed vector shows the star's proper motion of 45.4 mas yr^{-1} at PA = 194°, magnified by a factor of 10^4. (b) The FUV emission around W Hya over a large field of view, with major structural features marked. Dashed white circles show partial ringlike structures of radii 65″, 160″, and 220″. Several radial (compact as well as extended) features, likely corresponding to outflows, are labeled as A, B, ... G. Outflows A, B, and C show diametrically opposed pairs (denoted with subscripts 1 and 2, e.g., A_1 and A_2). Outflow G is inferred from the presence of diffuse emission regions (encircled with green ellipses) located roughly north of the star. Four large azimuthal structures are labeled T_1–T_4. Bright compact bright sources (labeled "g") are likely background galaxies. North is up and east is to the left. The scale bar shows intensity in cps pix^{-1}.
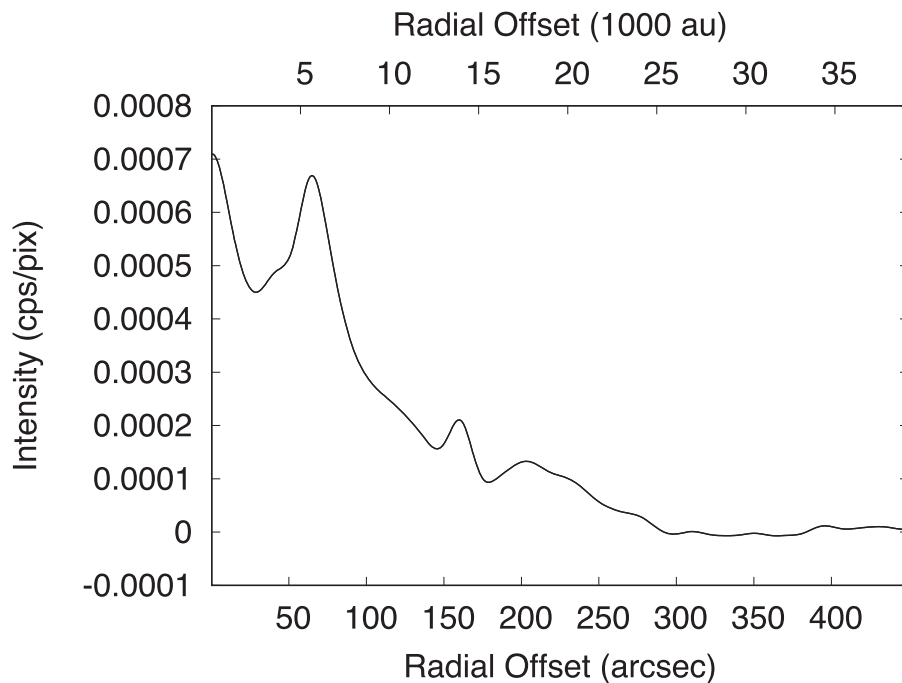

Figure 14. Radial intensity cut of the FUV emission around W Hya; intensity has been averaged over an azimuthal wedge with its apex centered on the star and covering the angular range PA = 95° to 235°. The average surrounding sky intensity has been subtracted from the cut.
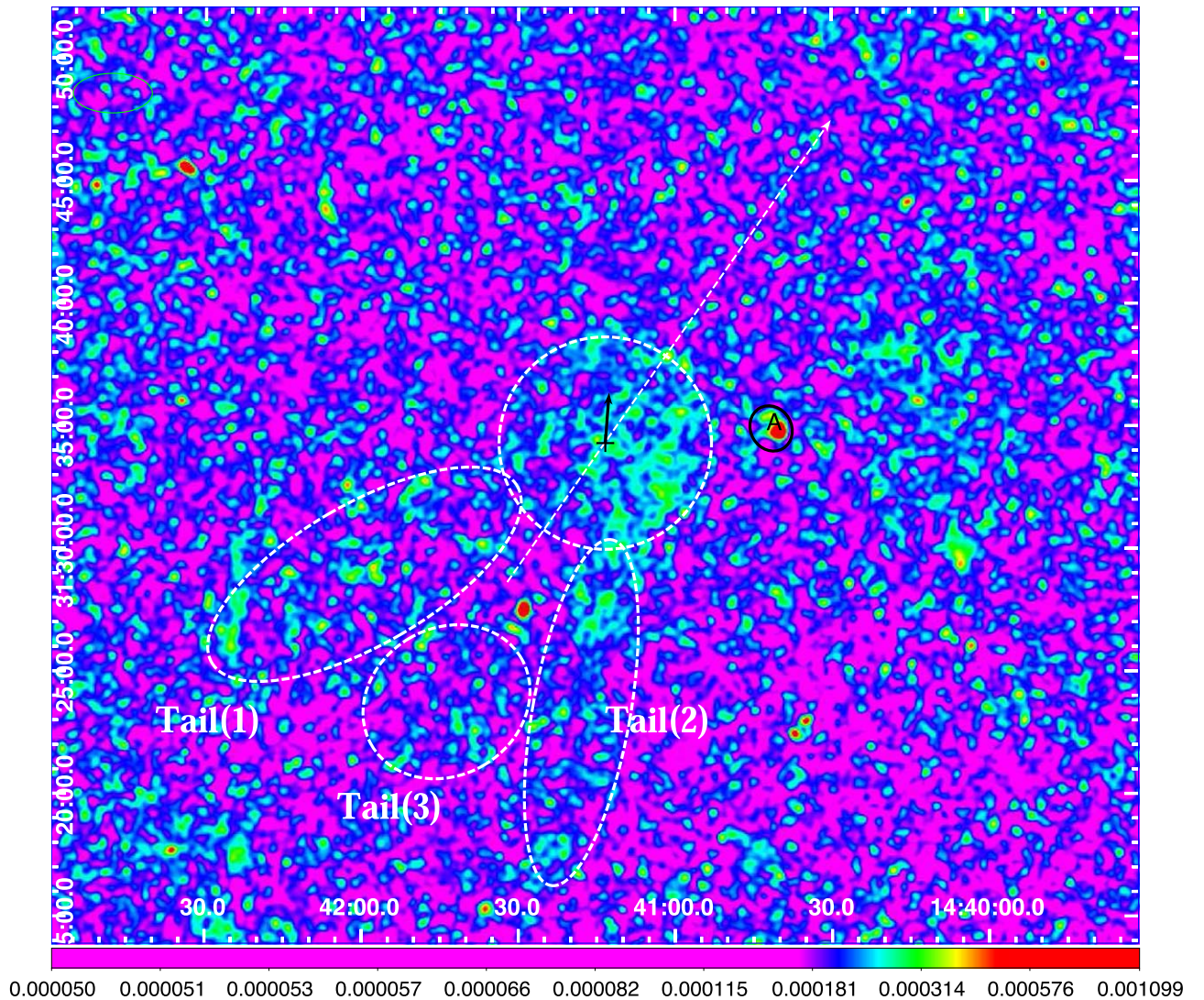
Figure 15. The FUV emission toward RW Boo, imaged with GALEX. The dashed white circle (radius 260″), delineates the radial extent of the termination shock in the astrosphere, seen to the west of RW Boo. Black vector shows the star's proper motion of 12.4 mas yr^{-1} at PA = 356°, magnified by a factor 10^4; white vector shows symmetry axis of the astrosphere. Region A (black ellipse) shows local environment around a bright point source that could not be adequately removed. North is up and east is to the left. The scale bar shows intensity in cps pix^{-1}.

We infer that the outermost (rather broad) radial intensity peak at $r \sim 220''$ corresponds to the interaction of W Hya's wind with the ISM. A plausible explanation of the innermost peak at $r = 65''$ is that it results from the interaction of a higher-expansion velocity episode of enhanced mass loss interacting with an older, lower-density, slower wind. Such a modification of mass-loss rate and expansion velocity can result from a thermal pulse and is the preferred explanation for the presence of the "detached" shells seen in a number of carbon stars (Olofsson et al. 2010 and references therein). The ring at $r = 160''$ may have a similar origin as the one at $r = 65''$.

3.8. RW Boo

The FUV image of RW Boo (Figure 15) shows relatively bright emission in a $\sim 180°$ wedge around PA $\sim -90°$, suggesting that the termination shock lies west of RW Boo with a east–west symmetry axis. This extended FUV emission structure has no counterpart in the NUV image. However, we also see faint tail structures southeast of the star, characterized by enhanced emission in patches labeled Tail(1), Tail(2), and Tail(3), suggesting that the symmetry axis of the astrosphere lies along PA $\sim -35°$. However, the proper motion vector is directed along PA $= -4°$, closer to the orientation of Tail(1), suggesting that the latter defines orientation of the symmetry axis.

Assuming that the symmetry axis is one that bisects the tail region, we have made a radial intensity cut averaged over an azimuthal wedge with is apex centered on the star, spanning the range from PA $= -75°$ to 5° (Figure 16). The cut shows a sharp peak at $r = 260''$ followed by a steep decline to the average sky background intensity at $r \sim 310''$—we therefore infer a termination-shock radius, i.e., $R_1 = 260''$, and an astrosheath outer radius of $R_c = 310''$. Radial intensity cuts assuming an east–west symmetry axis yield similar results.

There is a possible low-intensity region in the range $r \sim 310''$–$425''$ that likely represents emission from swept-up ISM material between the outer edge of the astropause and the bow-shock interface separating the shocked and unshocked ISM.
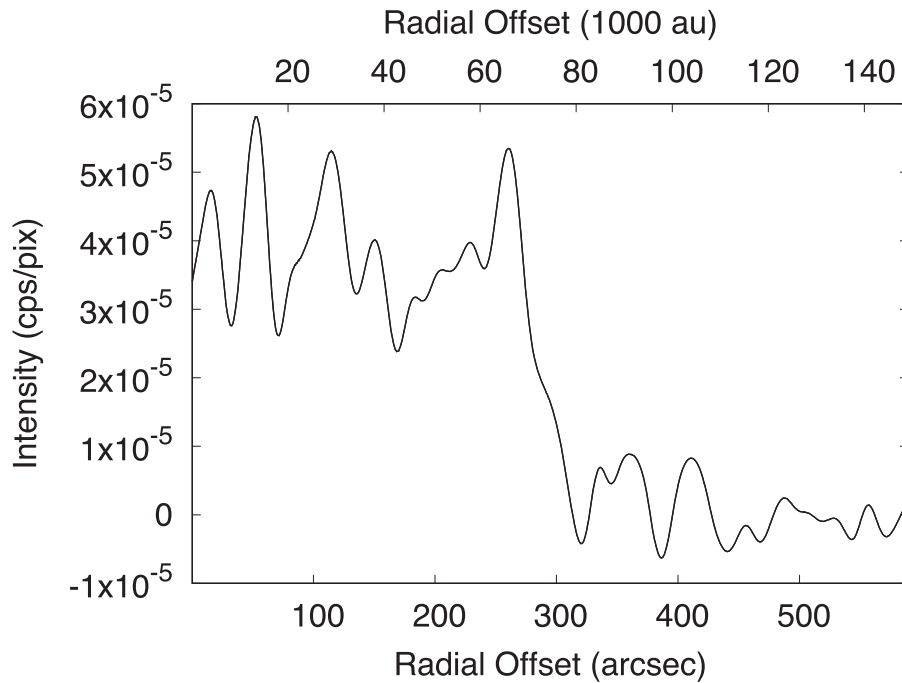
Figure 16. Radial intensity cut of the FUV emission around RW Boo; intensity has been averaged over an azimuthal wedge with its apex centered on the star, covering the angular range PA $= -75°$ to $5°$. The average surrounding sky intensity has been subtracted from the cut.

3.9. RX Boo

The FUV image of RX Boo (Figure 17) shows a bow-shock structure to the south-southeast side of the star. The symmetry axis of this structure is somewhat uncertain—one possibility is SymAx 1, at PA $\sim 170°$, which bisects the "nose" structure in the bow shock; a second possibility is SymAx 2, at PA $\sim 140°$, which bisects a spiny structure northwest of the star that may be the astrosphere's tail. The proper motion vector lies much closer to SymAx2 than SymAx1, suggesting that SymAx1 is the symmetry axis of the astrosphere.

We have made radial intensity cuts of the FUV emission around RX Boo, averaged over azimuthal wedges with their apexes centered on the star, and spanning the range from PA $= 150°$ to $190°$ (around SymAx 1) or PA $= 120°$ to $160°$ (around SymAx 2) (Figure 18)—these wedges avoid regions A and B, which result from imperfectly subtracted bright point sources. Both cuts show a broad hump centered at $r \sim 320''$. In the cut around SymAx 1 the hump has a peak at $r \sim 300''$, a local minimum, a more pronounced peak at $\sim 350''$, and then a steady decline. In the cut around SymAx 2, the hump shows a peak at $r \sim 300''$ followed by a steady decline at $r \gtrsim 340''$. An average of the two cuts shows two small peaks at $r = 300''$ and $r = 350''$ followed by a steady decline. We take the average of the locations of the two peaks as an estimate of the termination-shock radius, i.e., $R_1 = 325''$; the astrosheath outer radius is estimated to be $R_c = 460''$.

3.10. VX Eri

The FUV image of VX Eri (Figure 19) shows extended emission around the star. No such structure is seen in the NUV image. Unfortunately, VX Eri is located close to the edge of the FUV detector, so we are likely not seeing the full structure of the extended emission. The proper motion vector of VX Eri is directed toward PA $= -168°.6$. Hence, the emission that is seen

toward the northeast and north of the star may represent part of the astrosphere's tail. In this case, we would expect the termination-shock intensity to peak in the opposite direction, i.e., toward the south and southwest, but we mostly see bright emission in the southwest quadrant. We therefore consider the detection of an astrosphere around VX Eri as tentative. We have made a radial intensity of the FUV emission around VX Eri, averaged over an azimuthal wedge with its apex centered on the star, covering the azimuthal range PA $= 100°$ to $180°$ (Figure 20). The cut shows a broad peak at $r \sim 280''$, followed by a decrease in intensity at $r \sim 290''$, then a local minimum, and then a second peak at $r = 300''$, with a final steady decline to a plateau region starting at $r \sim 460''$. The background sky intensity is reached at $r \sim 580''$. We take the average of the two peaks near the edge of the bright UV region as a rough estimate of the radius of the termination shock, $R_1 = 290''$; the astrosheath outer radius is estimated to be $R_c = 460''$. The plateau region in the range $r \sim 475''$–$580''$ may represent emission from swept-up ISM material between the outer edge of the astropause and the bow-shock interface separating the shocked and unshocked ISM.

4. Astrospheres and Mass Loss

Out of the 92 objects with long-exposure (>700 s) FUV images examined for our survey, we found ten objects with extended FUV emission. In these objects, with the exception of V Hya, we find the typical shock morphology expected for a spherical wind moving relative to, and interacting with, the ISM in all objects (tentatively in VX Eri). For the latter, we find evidence of (i) its large parabolic outflows interacting with the ISM and (ii) its collimated, very high-velocity outflows interacting with the circumstellar medium. We exclude it from further discussion and the astrosphere analysis (below) because
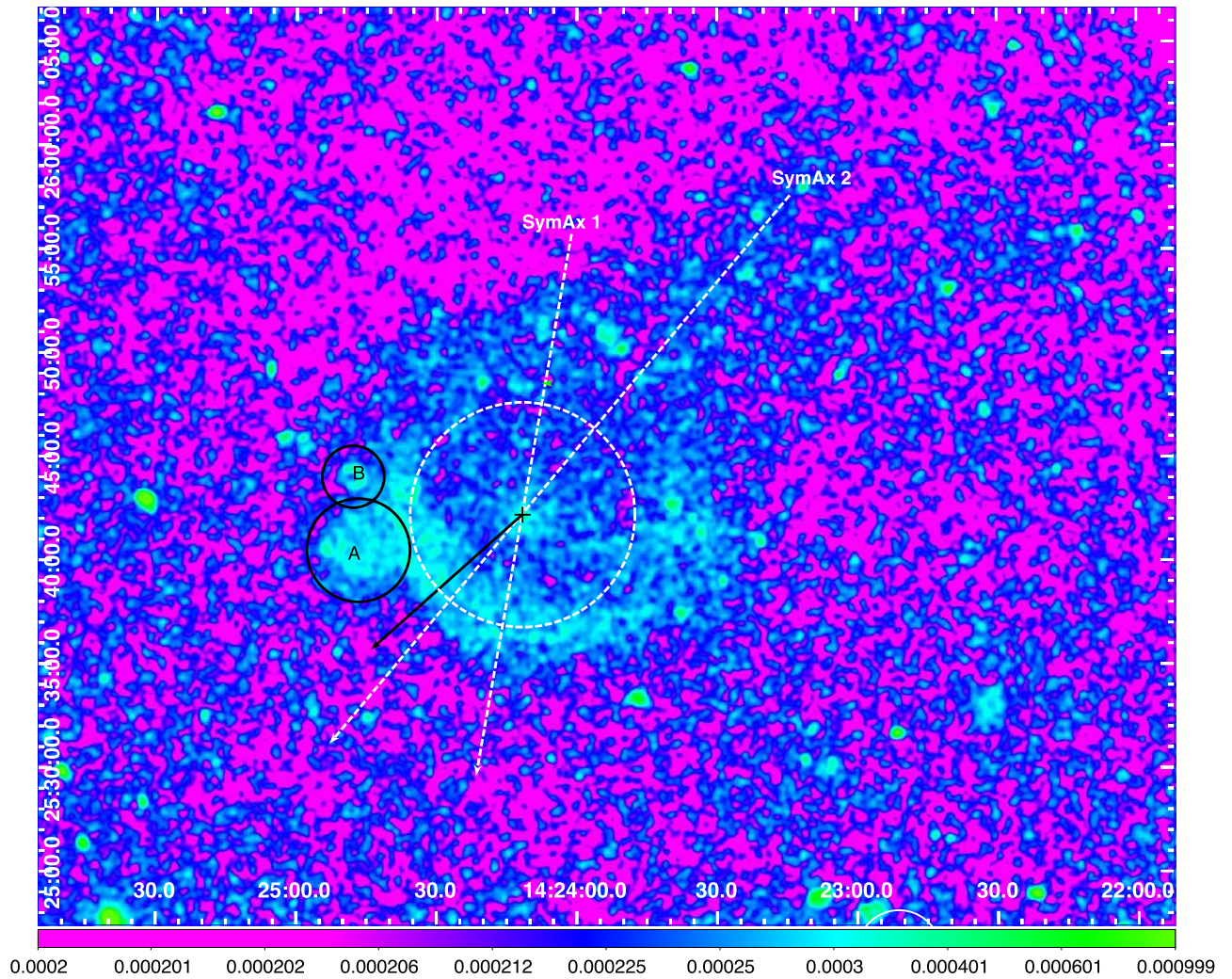
Figure 17. The FUV emission toward RX Boo, imaged with GALEX. The white dashed circle (radius 325″), delineates the radial extent of the termination shock in the astrosphere, south-southeast of RX Boo (black cross). The white dashed vectors labeled SymAx 1 and SymAx2 represent two possible symmetry axes of the astrosphere. Black vector shows the star's proper motion of 58.8 mas yr^{-1} at PA = 132°, magnified by a factor 10^4. "A" shows where a bright point source could not be removed; "B" shows a related ghost artifact. North is up and east is to the left. The scale bar shows intensity in cps pix^{-1}.

the wind−ISM interaction in it cannot be analyzed using the equations that govern a spherical wind−ISM interaction.

Excluding V Hya, eight out of the nine objects have relatively large proper motions, and we find, as expected, that the termination-shock region lies in a hemisphere that contains the proper motion vector. For five of these eight objects (EY Hya, RT Vir, R Hya, RW Boo, and RX Boo) the symmetry axis of the termination shock lies within $\lesssim\pm30°$ of the proper motion vector. Of the remaining three (U Ant, W Hya, and VX Eri), we do not have a full image of the astrosphere for VX Eri. For U Ant, the symmetry axis is quite uncertain (see Section 3.3), so the angle between the proper motion vector and the former could be anywhere in the range 20°–35°. W Hya is thus the only source with a large proper motion, where it is clear that the termination shock is brightest in an azimuthal wedge offset by more than ∼60° from the proper motion vector. This suggests that the ambient ISM material around W Hya has a significant streaming velocity directed roughly westwards; alternatively, our inference about its astrosphere is incorrect—we discuss this in more detail below (Section 4.2.2). We note that, like W Hya, the astrosphere of CIT 6 also displays a relatively large azimuthal offset between the proper

motion vector (PA = −60°; Figure 21) and the symmetry axis of the termination shock (PA ∼ 2°; Sahai & Mack-Crane 2014).

The proper motion of R LMi is relatively small (2.4 mas yr^{-1}) compared to the other objects (∼12″–79″; Table 2), consistent with the roughly circular shape of its astrosphere.

4.1. Detection Statistics and FUV Extinction

The fraction of AGB stars with wind−ISM interactions detected via emission in the GALEX FUV band[11] appears to be relatively low, ∼0.14, especially in comparison to far-IR observations, which is ∼0.4 based on the Cox et al. (2012) study. Although a full consideration of sample selection biases in our study and that of Cox et al. (2012) is outside the scope of this paper,[12] an obvious factor that makes it relatively more difficult to detect FUV emission than far-IR emission is interstellar extinction. This extinction depends both on the object's distance and the height above the Galactic plane, z. We have derived the broadband extinction in the GALEX FUV

_____

[11] Including the previously detected AGB stars, Mira, IRC+10216, and CIT 6.
[12] These biases will be discussed in detail in a follow-up paper that will cover the full survey.
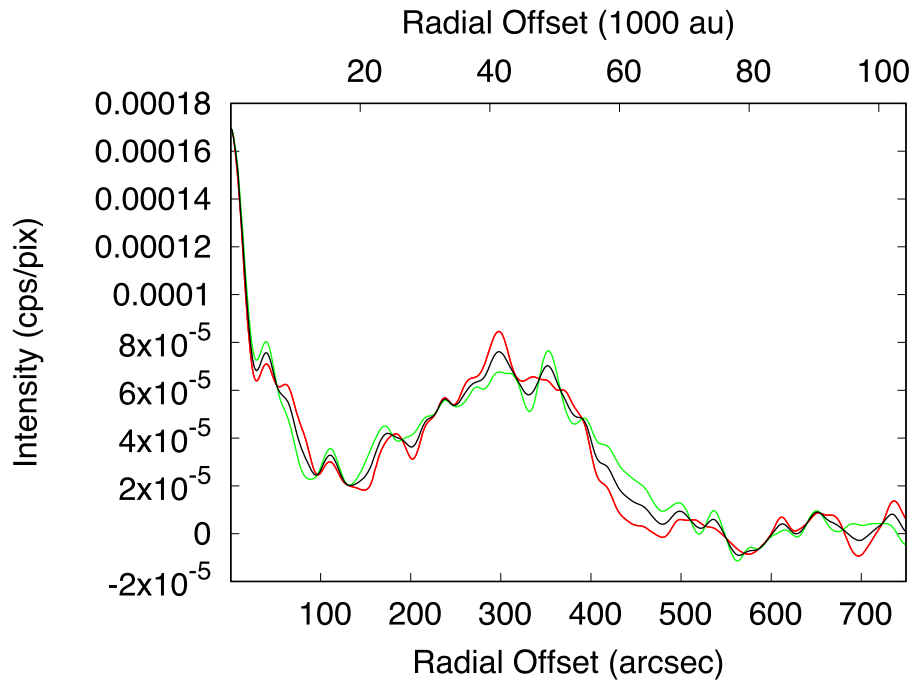
16

Figure 18. Radial intensity cuts of the FUV emission around RX Boo, averaged over azimuthal wedges with their apexes centered on the star, and spanning the range from PA = 150° to 190° (green curve), PA = 120° to 160° (red curve), and an average of the two (black curve). The average surrounding sky intensity has been subtracted from the cut.

band for all our survey sources as follows: (i) the visual extinction A_V for each source was computed using the the GALExtin[10] tool (Amôres et al. 2021), which estimates interstellar extinction based on both available 3D models/maps and distance (Amôres & Lépine 2005); (ii) the FUV extinction, A_{FUV}, was computed using the values of A_{FUV}/E_{B-V} and A_V/E_{B-V} for the Milky Way in Table 2 of Bianchi (2011). The distribution of A_{FUV} for the undetected objects peaks at ~0.25 (excluding a few outliers), with a full-width at half-maximum of 0.25, thus not significantly different from that for our small sample of detected objects. Hence, it is unlikely that FUV extinction is the primary reason for the nondetection of FUV emission in the majority of the survey sample. More likely, other parameters that affect the presence and brightness of the wind−ISM interaction may be responsible such as the past history of mass loss on long timescales (~10^5 yr), the relative motion between the star and the ISM, and the local ambient density of the ISM (see below).

4.2. Analysis of the Wind−ISM Interaction

We now use our estimates of the radius of the termination shock and the thickness of the astrosheath (listed in Table 2) for each of our targets where we can identify such structures to derive various parameters characterizing the mass-ejection history in these objects, following the methodology described by Sahai & Mack-Crane (2014). These parameters, listed in Table 3, include the relative velocity between the star and the ISM (col. 14); the duration of, and total mass in, the unshocked wind (cols. 15–16); the duration of, and total mass in, the shocked wind (cols. 15–16); and the total ejected mass (col. 19), together with additional parameters relevant for the derivation of these parameters. We have adopted distances to our targets from Andriantsaralaza et al. (2022) and when those

are not available, from Bailer-Jones et al. (2021; col. 2, Table 3). The mass-loss rates in Table 2 have been scaled to (i) the adopted distances and to (ii) a common value of the CO-to-H_2 abundance ratio—3×10^{-4} for O-rich stars, and 10^{-3} for C-rich stars (col. 12, Table 3). The largest uncertainty in the analysis described below is due to (i) uncertainties in the mass-loss rates and (ii) assuming that the mass-loss rates and expansion velocities are constant with time.

In brief, we estimate the star's relative velocity V_* through the surrounding ISM using the relationship between l_1, the distance of the termination shock from the star along the astropause's symmetry axis (i.e., the termination-shock stand-off distance), and V_* using Equation (1) in van Buren & McCray (1988). We reproduce this equation below for convenience, as given in Sahai & Mack-Crane (2014), who made a correction to the original equation (missing minus sign in the exponent of $\bar{\mu}_H$ in Equation (1) of van Buren & McCray 1988):

$$l_1(\mathrm{cm}) = 1.74 \times 10^{19} (\dot{M}_{*,-6} V_{w,8})^{1/2} (\bar{\mu}_H \, n_{ISM})^{-1/2} V_{*,6}^{-1}, \quad (1)$$

where $\dot{M}_{*,-6}$ is the stellar mass-loss rate in units of 10^{-6} $M_\odot \, \mathrm{yr}^{-1}$, $V_{w,8}$ is the wind velocity in units of $10^3 \, \mathrm{km \, s^{-1}}$, $\bar{\mu}_H$ is the dimensionless mean molecular mass per H atom, and n_{ISM} is the ISM number density in cm^{-3}.

We make the simplifying assumption that the astropause's symmetry axis lies in the sky plane, i.e., the inclination angle, $\phi = 90°$; hence $l_1 = R_1$. We estimate the density of atomic and ionized hydrogen near each object (cols. 8–9, Table 3) based on its location in the Galaxy (i.e., Galactocentric radius R and height z above the Galactic plane, cols. 5–6, Table 3) as described by Sahai & Mack-Crane (2014) using published models (Gaensler et al. 2008; Kalberla & Kerp 2009) and sum them to estimate the total ISM density. The duration (P_w) of, and total mass (M_w) in, the unshocked wind (i.e., within $r \leqslant R_1$) is estimated from the mass-loss rate and expansion velocity of
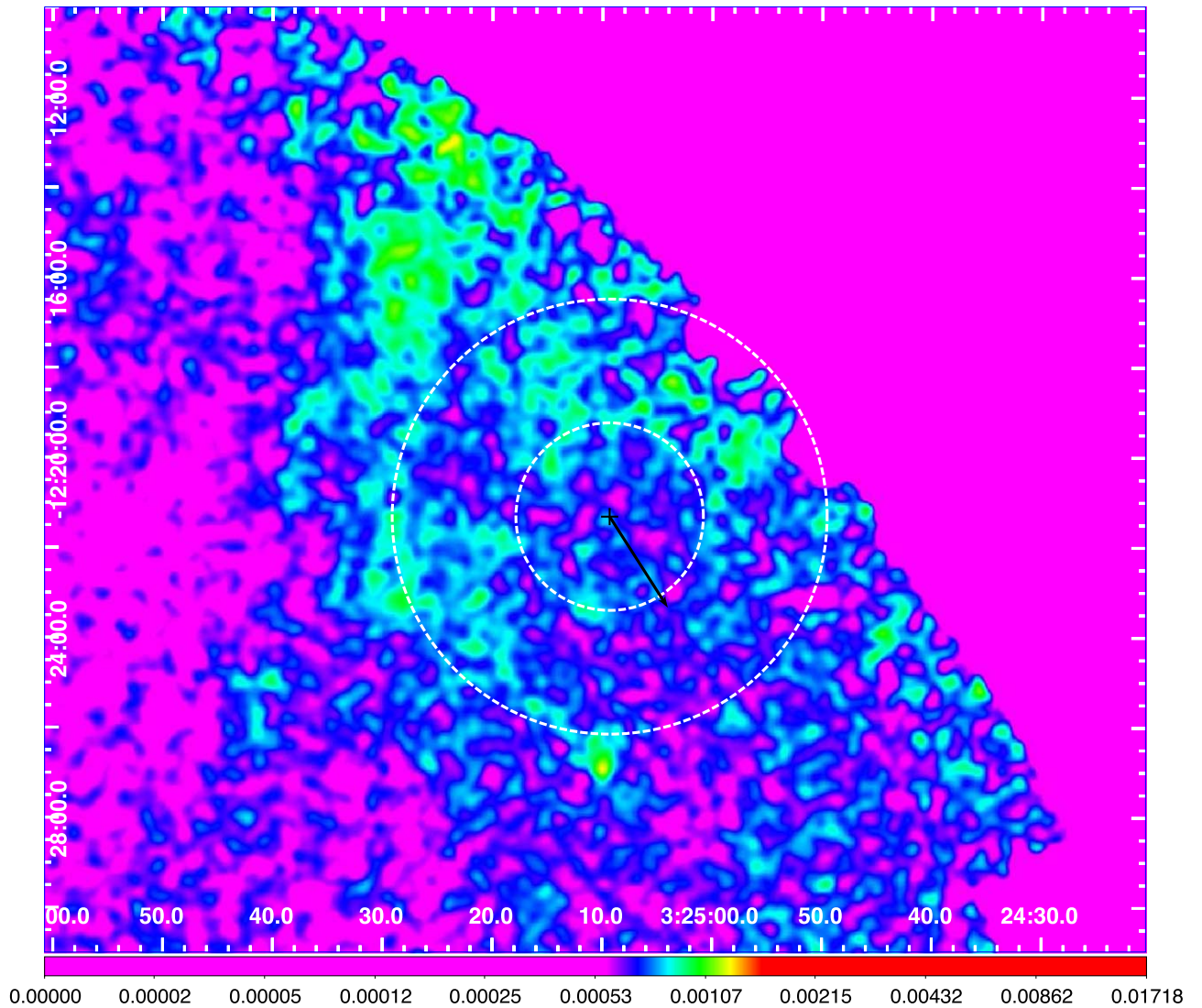

Figure 19. The FUV emission toward VX Eri, imaged with GALEX. The dashed white circle (radius 290″), delineates the radial extent of the termination shock in the astrosphere, southeast of VX Eri. Black vector shows the star's proper motion of 14.4 mas yr^{-1} at PA = 213°, magnified by a factor of 10^4. North is up and east is to the left. The scale bar shows intensity in cps pix^{-1}.

the unshocked wind. The duration of mass loss corresponding to the shocked wind in the astropause ($R_1 < r < R_c$), P_s, is estimated using its width ($R_c - R$) and an estimate of the expansion velocity in this region, V_s, assuming that the shock is adiabatic (see Sahai & Mack-Crane 2014 for details). The values for P_s are likely to be lower limits for objects in which the astrosheath width, as a fraction of the termination-shock radius, $(R_c - R_1)/R_1$, is significantly less than 0.47, expected for the adiabatic case (see Equation (2) of van Buren & McCray 1988).

4.2.1. Velocity of Stars Relative to the Local ISM

We compare the values of the relative velocities between the stars and their local ISM, V_* (derived from our analysis above) to their peculiar space velocities, V_t (derived using their local standard-of-rest (LSR) radial velocities from CO millimeter-wave line observations, tangential proper motions from GAIA DR3, and distances). We have corrected V_t for solar motion $v_\odot$ [$(U, V, W) = (8.5, 13.38, 6.49)$ km s^{-1}] (Coşkunoğlu et al. 2011). We also assume, as in Cox et al. (2012), that the local

ISM for each star is at rest relative to the LSR—this is a simplification for cases where the ISM may have a significant flow relative to the LSR, e.g., due to the presence of expanding super-bubbles (e.g., as found for α Ori by Ueta et al. 2008).

We find that for five objects, EY Hya, R LMi, U Ant, RT Vir, and R Hya, there is reasonable agreement between V_* and V_t (i.e., within a factor $\lesssim 2$), considering (i) the uncertainties in the mass-loss rates based on CO data, $\dot{M}_{w,0}$, which is easily a factor few (due to uncertainties in a variety of factors, such as the CO-to-H_2 abundance ratio and the outer radius of the CO-emitting CSE, together with the use of empirical formulae or models that do not properly account for heating-cooling processes that determine the radial kinetic temperature distribution Sahai 1990) and (ii) intrinsic variations in the mass-loss rate over the very long periods (typically $\sim 10^5$ yr; see below) probed by the UV data. However, the discrepancies between V_* and V_t for the other four objects—VX Eri, W Hya, RW Boo, and RX Boo—are much larger although we may exclude VX Eri in this comparison since we classify it is astrosphere as a tentative detection, and its gas mass-loss rate (expansion velocity) is unknown and estimated from the dust-
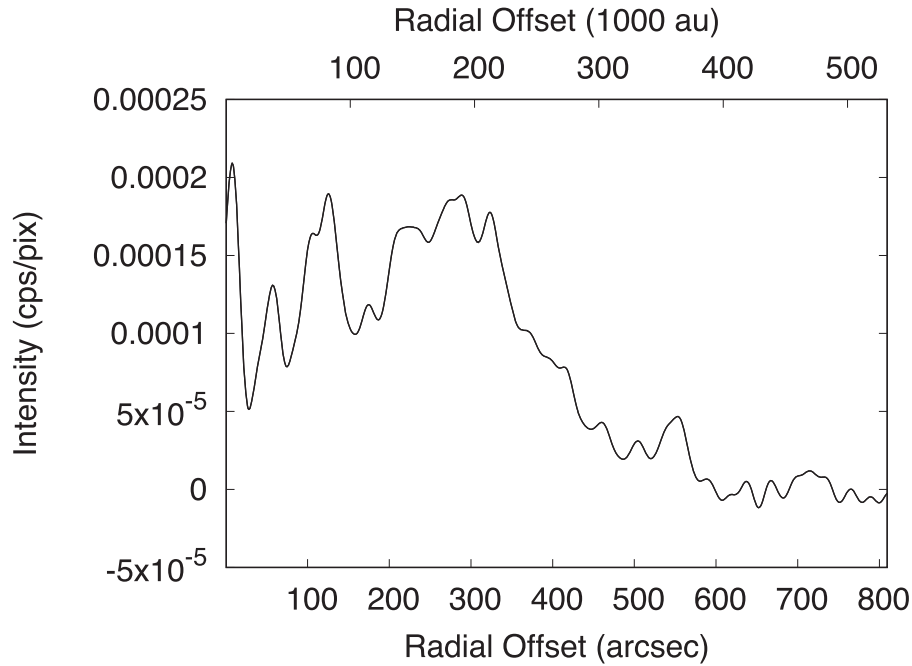
Figure 20. Radial intensity cut of the FUV emission around VX Eri; intensity has been averaged over an azimuthal wedge with its apex centered on the star and covering the angular range PA = 100° to 180°. The average surrounding sky intensity has been subtracted from the cut.

mass loss rate (with an assumed gas-to-dust ratio). Since V_* scales as $(\dot{M} \, V_e)^{1/2}$, and given that V_e can be determined fairly reliably (typically to $\pm 15\%$ or better) from the CO line profiles, relatively large changes in $\dot{M}$ ($\gtrsim 10$) are required to make V_* comparable to V_t. We note that for six out of nine stars with astrospheres, V_* is less than V_t, suggesting that $\dot{M}$ was significantly higher in the past.

4.2.2. Duration of Mass-loss and Total Ejected Mass

Our results show, that as for IRC+10216 and CIT 6, the FUV emission traces the AGB stellar wind in our objects to much larger distances from the star and therefore probes a much longer history of mass loss than typical mass-loss indicators such as CO millimeter-wave line emission which becomes undetectable due to photodissociation by the interstellar UV field, at radii typically $\lesssim 2 \times 10^{17}$ cm (or less) even for mass-loss rates as high as $\sim 10^{-5} \, M_\odot \, \text{yr}^{-1}$, hence probing mass ejection over a mere 6500 yr (assuming a typical expansion velocity of 10 km s^{-1}). Far-IR observations can similarly probe the very extended mass-loss histories (e.g., Cox et al. 2012 and references therein), but these are sensitive to a minor component of the mass ejecta, i.e., dust. We compare the FUV and far-IR results for the six objects that are common between our study and the far-IR studies (U Ant, R Hya, W Hya, RT Vir, V Hya, and RX Boo).

For two of these (U Ant, R Hya), we find that the wind−ISM interaction region lies at a significantly larger radius than could be seen in the far-IR data. In U Ant, the shell seen at $r \sim 42''$ in the far-IR is due to a wind–wind interaction; we find, from the FUV data, a wind−ISM interaction region at $r \sim 175''$. In R Hya, a shell at $r = 93''$ is seen in the far-IR; we find, from the FUV data, a wind−ISM interaction region at $r \sim 120''$.

In W Hya, a shell at $r = 93''$ is seen in the 70 and 160 μm imaging and a more distant one at $r \sim 230''$ only at 160 μm; the latter corresponds to the radius of the termination shock that we find from the FUV data. In RT Vir,

Maercker et al. (2022) derive a termination-shock radius of $85''$ from the far-IR imaging,[13] whereas the FUV data shows it to be smaller ($65''$).

In V Hya and RX Boo, Cox et al. (2012) did not find any emission related to a wind–wind or wind−ISM interaction.

We find that the duration of and total mass in the shocked wind (P_s, M_s) are significantly larger than their corresponding values (P_w, M_w) for the unshocked wind for all nine objects that show a wind−ISM interaction—this result is qualitatively consistent with that derived in the study by Maercker et al. (2022), who have modeled the far-IR data from Cox et al. (2012) to derive dust masses in the interaction regions, and made estimates of the crossing time (time taken for material to reach the interaction region, therefore equivalent to P_w) and buildup times (time taken by stellar wind to build up the mass in the interaction region, therefore equivalent to P_s). Comparing results for the three objects with wind−ISM interaction that are common between Maercker et al. (2022) and our study, we find that P_s/P_w for RT Vir, R Hya, and W Hya is 5.5, 2.5, and 3.8, compared to 2.9, 2.6, and 12.5, respectively, from Maercker et al. (2022).[14]

For five out of nine objects (EY Hya, R LMi, R Hya, W Hya, and RX Boo), the values of $(R_c - R_1)/R_1$ are significantly less than 0.47 (Table 2), showing that the shocked gas has cooled down significantly—hence, V_s is less than the adiabatic value, and the value of P_s, and consequently, M_s and M_t for these objects (Table 3) are lower limits.

It is instructive to compare the total ejecta masses (M_t) that we derive for our sample of AGB stars to the mass that needs to be ejected before an AGB star begins its post-AGB journey, which is $\gtrsim 0.5 \, M_\odot$ for stars with MS progenitor masses of $\gtrsim 1 \, M_\odot$ (Miller Bertolami 2016). We find that for all objects,

---

[13] Although Cox et al. (2012) detected the wind−ISM interaction for this object, they did not provide a value for the termination-shock radius.
[14] We exclude U Ant in this comparison since it does not show the wind−ISM interaction in the far-IR.
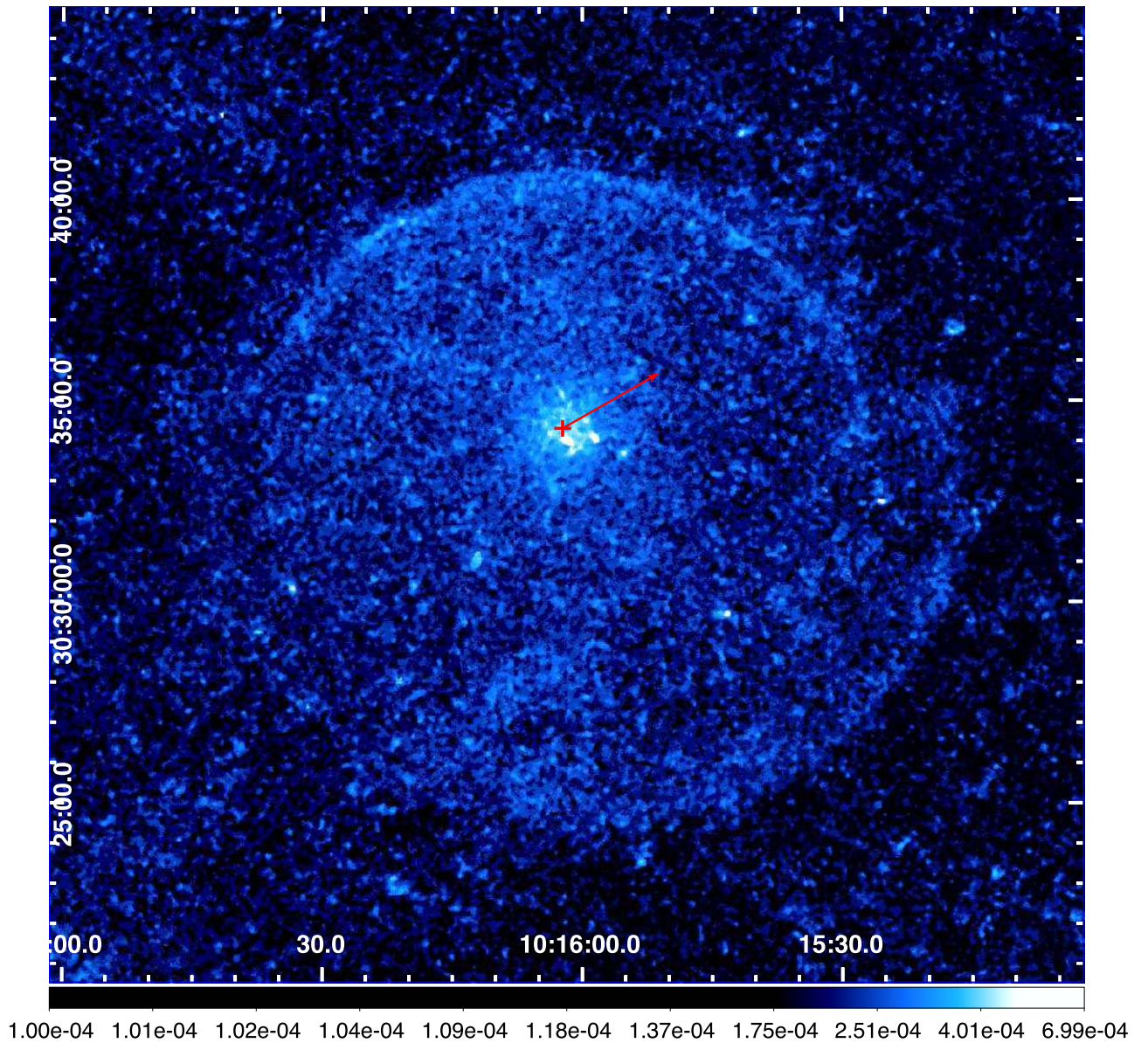
Figure 21. The FUV emission toward CIT 6, imaged with GALEX (adapted from Sahai & Mack-Crane 2014). Red vector shows the star's proper motion of 16.6 mas yr^{-1} at PA = 300°, magnified by a factor of 10^4; red cross shows the star's location. North is up and east is to the left. The scale bar shows intensity in cps pix^{-1}.

except U Ant, $M_t \ll 0.5\ M_\odot$. This suggests that these stars are still far from the end of their AGB lifetimes. Even if the mass-loss rates were significantly higher in the past for the five stars where we find $V_t > V_*$ (i.e., EY Hya, R Hya, W Hya, RW Boo, and RX Boo; we exclude VX Eri in this consideration for reasons above. See Section 4.2.1), and we scale up the mass-loss rate for these in order to make $V_* = V_t$, the scaled-up values of M_t are still significantly below $0.5\ M_\odot$. Although for four out of five of these stars, the value of M_t is likely a lower limit because the actual value of the shock velocity V_s is likely lower than the one derived assuming no cooling (see Section 4.2); only for one of these (EY Hya) is the scaled-up value of M_t high enough ($0.17\ M_\odot$) that a further increase resulting from a plausible decrease in V_s due to cooling could raise it to $\sim 0.5\ M_\odot$.

The remaining three stars (R LMi, U Ant, and RT Vir) have $V_t < V_*$; hence the mass-loss rate, and thus M_t, would have to be lower in order for $V_* = V_t$. U Ant is a carbon star and

believed to have descended from a progenitor of mass $3.6\ M_\odot$, slightly above the average of the range of progenitor masses of carbon stars (2.5–$4\ M_\odot$; Kastner & Wilson 2021), and so even though for it, $M_t \sim 1\ M_\odot$, it is also not close to transitioning to the post-AGB phase. Among the other two C stars with previously detected astrospheres in the UV, IRC+10216 and CIT 6, only IRC+10216 shows a large enough ejecta mass ($\sim 1.4\ M_\odot$; Sahai & Chronopoulos 2010) that it can be considered very close to transitioning to the post-AGB evolutionary phase.

The morphology of the FUV emission toward W Hya is remarkable, showing an unprecendented variety of azimuthal and radial structures, and indicating a fairly complex mass-loss history that includes multiple spherical and collimated outflows. The presence of collimated outflows is surprising, considering that these generally manifest themselves during the very late AGB or the early post-AGB phase, i.e., the pre-planetary nebula phase (e.g., Sahai & Trauger 1998;

Table 3
Physical Properties of Astrospheres

Name (1)[a]	Dist. (2)	$A_{\rm FUV}$ (3)	FUV Int. (4)	R (5)	z (6)	h_z (7)	n(H I) (8)	n(H$_+$) (9)	R_1 (10)	$R_c - R_1$ (11)	$\dot{M}$ (12)	V_t (13)	V_* (14)	P_w (15)	M_w (16)	V_s (17)	P_s (18)	M_s (19)	M_t (20)
VX Eri	0.657	0.38	1.6e-19	8.722	−0.512	0.156	0.000	0.122	191	112	0.023	51	2.3	90322	0.0021	0.83	635368	0.015	0.017
EY Hya	0.422	0.44	8.1e-20	8.600	0.186	0.154	0.301	0.234	54.9	16.9	0.33	32	15	23642	0.0078	0.92	87295	0.029	0.037
R LMi	0.320	0.53	3.6e-20	8.533	0.244	0.153	0.145	0.209	94.4	25.6	0.244	3.6	7.7	59668	0.015	0.62	194174	0.047	0.062
U Ant	0.294	0.36	3.8e-19	8.304	0.082	0.150	0.738	0.289	51.5	23.5	12.8	50	95	12837	0.16	1.58	70420	0.9	1.1
V Hya	0.311	0.34	3.9e-20	8.339	0.172	0.150	0.361	0.241	…	…	…	…	…	…	…	…	…	…	…
RT Vir	0.227	0.19	4.3e-20	8.275	0.210	0.149	0.231	0.223	14.8	6.81	0.929	47	86	8968	0.0083	0.65	49667	0.046	0.054
R Hya	0.126	0.094	5e-20	8.262	0.079	0.149	0.757	0.290	15.1	3.15	0.122	35	25	5734	0.0007	1.04	14335	0.0017	0.0024
W Hya	0.087	0	6.9e-20	8.276	0.047	0.149	0.854	0.309	19.1	6.09	0.0364	52	8.6	10675	0.00039	0.71	40758	0.0015	0.0019
RW Boo	0.253	0.22	3e-20	8.264	0.231	0.149	0.175	0.214	65.8	12.7	0.0299	19	5.6	18025	0.00054	1.44	41596	0.0012	0.0018
RX Boo	0.139	0.088	4.5e-20	8.289	0.130	0.149	0.540	0.262	45.2	20.9	0.0765	35	7.3	19121	0.0015	0.93	105901	0.0081	0.0096

Note.

[a] Column headings: (1) Name, (2) Adopted Distance to star (kpc)—from Andriantsaralaza et al. (2022) for R LMi, U Ant, V Hya, RT Vir, R Hya, W Hya, and RX Boo; from Bailer-Jones et al. (2021) for VX Eri, EY Hya, and RW Boo, (3) Interstellar Extinction in the GALEX FUV band, (4) Average FUV Intensity at Termination Shock (erg s^{-1} cm^{-2} Å^{-1} arcsec^{-2}), (5) Galactocentric Radius (kpc), (6) Height above Galactic Plane (kpc), (7) Disk Scale Height of Atomic Hydrogen (kpc), (8) Atomic Hydrogen Density (cm^{-3}), (9) Ionized Hydrogen Density (cm^{-3}), (10) Termination Shock Distance (10^3 au), (11) Thickness of Astropause (10^3 au), (12) Mass-Loss Rate, scaled to distance in Col. 4 (10^{-6} $M_\odot$ yr^{-1}), (13) Star velocity from radial velocity and tangential proper motion (km s^{-1}), (14) Star velocity relative to local ISM (km s^{-1}), (15) Duration of unshocked wind (yr), (16) Mass of unshocked wind ($M_\odot$), (17) Expansion Velocity of shocked wind (km s^{-1}), (18) Duration of shocked wind (yr), (19) Mass of shocked wind ($M_\odot$), (20) Total Mass (unshocked +shocked) ($M_\odot$).

Sahai et al. 2011), whereas, based on the small inferred value of ejected mass in it, W Hya is still very far from the end of its AGB lifetime. A possible solution to this predicament is that W Hya is actually near the end of its AGB lifetime and that its wind−ISM interaction region lies at a much larger radius than inferred from our current analysis but is too faint to be seen. In this scenario, R_1 (and thus l_1) would be larger, and the past mass-loss rate would have to be much higher in order to reconcile the value of V_* with V_t—e.g., with R_1 (and R_c) a factor of 2 larger, the value of M_t would be $\sim 0.55\,M_\odot$ (or even higher if V_s was lower than its adiabatic value.)

4.3. Comparison with Theory

Our FUV imaging enables us to detect an important component of the wind–ISM interaction that is expected from theory but cannot be distinguished in the far-IR studies of astrospheres—namely, the region between the outer edge of the astropause and the bow-shock interface separating the shocked and unshocked ISM. As noted earlier, in five objects (VX Eri, EY Hya, U Ant, RT Vir, and VX Eri) we can see a faint FUV emission "plateau" from this region in the radial intensity cuts, which lies just beyond the region of steeply declining intensity that characterizes the astrosheath. This faint emission likely arises in the shocked ISM. Such bow-shock emission has also been found in the astrospheres of IRC+10216 (Sahai & Chronopoulos 2010) and CIT 6 (Sahai & Mack-Crane 2014).

We note that while the FUV emission from some of the astrospheres found in our study shows the expected limb-brightened appearance as seen in IRC+10216 and CIT 6 (e.g., R LMi, U Ant, RX Boo, and possibly VX Eri), the others show a "filled" appearance, i.e., the average brightness of the emission interior to the termination-shock is comparable to that at the shock (EY Hya), or in fact rises inwards (RT Vir, R Hya, and W Hya).[15] The "filled"' objects may result from various kinds of hydrodynamic fluid instabilities revealed in numerical simulations of the wind−ISM interaction.

The FUV data on wind−ISM interactions presented in our study can be very useful for providing strong constraints on numerical hydrodynamical simulations of such interactions. Many such studies have been undertaken in the past with pioneering work by Blondin & Koerwer (1998) and Comeron & Kaper (1998), in which the morphology and dynamical evolution of wind bow shocks produced by runaway stars in the diffuse ISM were analyzed. Blondin & Koerwer (1998) examined the instabilities of isothermal stellar wind bow shocks and concluded that ragged, clumpy bow shocks should be expected to surround stars with a slow, dense wind, which is moving through the ISM with a Mach number greater than a few (i.e., with relative velocity of order $60\,\mathrm{km\,s^{-1}}$). Comeron & Kaper (1998) found a diversity of structures, even with moderate changes in basic input parameters: depending on these, the bow shocks may have a simple or layered structure or may not even form at all.

In the case of AGB astrospheres, such simulations can be used to explore the effects on the astrospheres of varying physical parameters of the stars (mass-loss rate, wind velocity, and velocity relative to the ISM, including time variations) and the ambient ISM (density, temperature) systematically on the detailed shape and structure of the astrosphere in both gas and

dust. The combination of the FUV imaging presented here, together with the far-IR imaging, provides a unique database for the study of wind–wind and wind−ISM interactions.

A unique strength of simulations is that they enable one to utilize the information present in the microstructure of the shocks. Such structure can result from different kinds of fluid instabilities, such as Rayleigh–Taylor (RT) and Kelvin–Helmholtz (KH) instabilities. RT instabilities can be quenched by a magnetic field; thus the presence and/or absence of RT fingers can be used to set constraints on the presence of a magnetic field. The KH instability together with the RT instability can form mushroom-shaped structures on the ends of RT fingers. KH time-dependent turbulent eddies can become large enough to affect the large-scale morphology of the shocked gas. Other instabilities include the nonlinear thin shell instability (Vishniac 1994), the transverse acceleration instability (Dgani et al. 1996), and large-scale vortex instabilities (Wareing et al. 2007).

The above simulations can be made more useful by including relevant physical processes such as heating and cooling. Treating the gas and dust as separate fluids and accounting for dust charge/size distribution and destruction is especially important for modeling the far-IR data. Cox et al. (2012) have carried out seven simulations (without dust radiative cooling, charge, or destruction) in order to determine how the morphology of the bow shock varies with various stellar wind and ISM properties. Villaver et al. (2012) present another set of pure hydro simulations but include wind modulations prescribed by stellar evolution calculations and cover a range of expected relative velocities (10–$100\,\mathrm{km\,s^{-1}}$), ISM densities (0.01–$1\,\mathrm{cm^{-3}}$), and stellar progenitor masses (1 and $3.5\,M_\odot$). Such studies are most useful when accompanied by observational predictions, e.g., the hydrodynamical modeling of α Ori's astrosphere by Mohamed et al. (2012).

5. The H_2 Line Spectrum of an Astrosphere and Future Spectroscopic Observations

One of the major limitations of the FUV data as a probe of wind–wind or wind-ISM interactions is that no spectra of the FUV emission are available to confirm the current hypothesis for the nature and origin of the emission[16]—collisional excitation of the H_2 Lyman–Werner band line emission by hot electrons in shocked gas. This hypothesis is based on modeling of very low-resolution grism spectroscopy of the FUV emission from Mira's astrosphere by Martin et al. (2007) —no spectra showing actual lines could apparently be extracted against the diffuse FUV background.[17] A full understanding of the nature of FUV emission from astrospheres requires high-resolution ($R \sim 100{,}000$) spectroscopic observations.

We use a simple model of the FUV emission resulting from electron impact excitation of H_2 in order to estimate the expected spectrum from an astrosphere. We generate a model spectrum using a code written by Dr. X. Liu (Space Environment Technologies)[18] (Liu & Dalgarno 1996a, 1996b) for electron impact energy 100 eV (the spectrum is relatively insensitive to

---

[15] While making this inference, we have disregarded the sharp central peak that can be seen in some objects.

[16] The far-IR data suffer from a similar limitation since the [O I]63 μm and [C II]158 μm line emission may contribute to the emission seen in the broadband PACS 70 and 160 μm filters used in the far-IR observations by Cox et al. (2012).

[17] The spectral fits shown in their Figure S3 are model fits to the spatial intensity in the grism image.
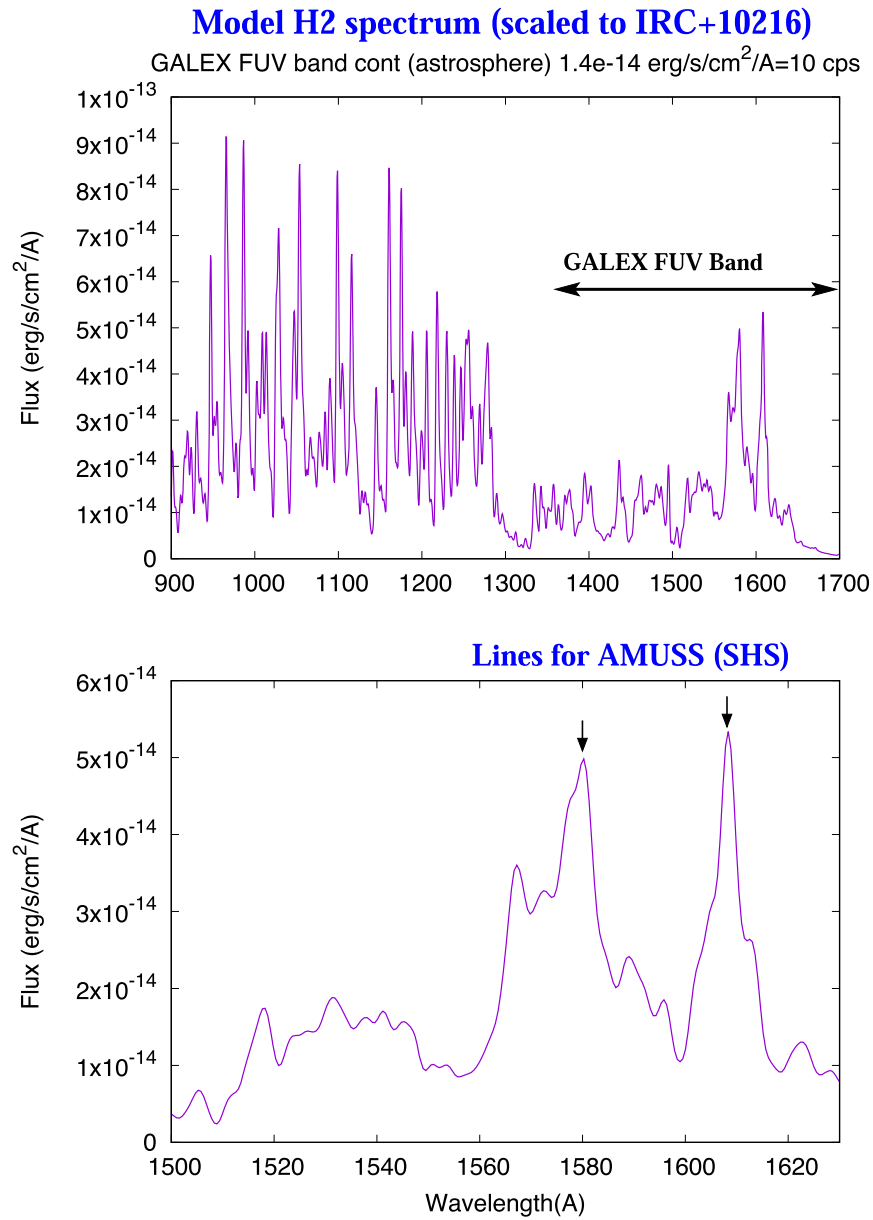
[18] Code has been updated in 2019.

Figure 22. A model FUV-band spectrum due to electron impact excitation of H_2, scaled to fit the FUV emission flux observed in an elliptical patch of size $210'' \times 110''$ covering the brightest part of the leading edge of the astrosphere of IRC+10216. Top panel shows the full spectrum of Lyman–Werner band lines, whereas the bottom panel shows an expanded view of the spectrum indicating the centers of two wavelength windows that would be optimum for observations with AMUSS.

this energy) and H_2 rotational temperature 300 K. This spectrum is then convolved with the GALEX FUV band response and scaled in order to reproduce the broadband GALEX FUV flux emitted by an astrosphere (in $\text{erg s}^{-1}\,\text{cm}^{-2}\,\text{Å}^{-1}$ or cps, where 1 $\text{cps} = 1.4 \times 10^{-15}$ $\text{erg s}^{-1}\,\text{cm}^{-2}\,\text{Å}^{-1}$). Using this model, we compute the spectrum of the FUV emission from the astrosphere of IRC+10216. We extracted the total flux (10 cps) from an elliptical patch of size 210×110 pix^2 (A_{shs}) covering the brightest part of the leading edge of the astrosphere of IRC +10216 and then obtained a prediction of the astrosphere spectrum (Figure 22) as described above.

The Cyclical Spatial Heterodyne Spectrometer (SHS) can provide the sensitivity required to obtain high-resolution spectra of this faint line emission from IRC+10216's astrosphere in particular and the astrospheres of AGB stars in general—a sensitivity that traditional slit spectrographs lack.

This interferometric instrumental technique, conceived at the University of Wisconsin in the 1990s and built and tested in the laboratory at visible and UV wavelengths, demonstrated concept-feasibility and performance characteristics (Harlander et al. 1992). Radial velocity resolved detections of interstellar [O II]3727 line emission were obtained by Mierkiewicz et al. (2006, 2007) from the University of Wisconsin's Pine Bluff Observatory using an SHS. Payload performance at 1550 Å of an SHS on board a sounding rocket has also been tested (Watchorn et al. 2010).

SHS employs a miniature all-reflective two-beam interferometric technique to obtain spectra at a very high spectral resolving power ($R \sim 100{,}000$) of light collected from a large diffuse, faint emission region (Dawson & Harris 2009; Hosseini & Harris 2012, 2020; Hosseini 2019). Field testing carried out by Corliss et al. (2015) has demonstrated that

reflective SHS instruments can deliver effective interferometric performance in the visible to FUV wavelengths with commercial optics of moderate surface quality. The Astrophysics Miniaturized UV Spatial Spectrometer (AMUSS) concept, submitted in response to RFI NNH17ZDA010L: Possible NASA Astrophysics SmallSats, utilizes such an instrument (with mass <5.4 kg for three different UV lines served by three SHS instruments) that when coupled to a small-aperture ($\lesssim 30$ cm) space-based telescope, can provide high-resolution spectra of diagnostic UV lines emitted by extended, faint astrophysical objects, such as astrospheres, the ISM in our galaxy, and the circumgalactic medium in nearby galaxies (Hosseini & Sahai 2019).

The lower panel of Figure 22 shows an expanded view of the spectrum of IRC+10216's astrosphere, with black arrows indicating the centers of two wavelength windows covering lines that would be optimum for observations with AMUSS. Although there is a plethora of strong lines at shorter wavelengths ($\lesssim 1300$ Å), AMUSS would be less sensitive to them because of the steep decrease in the quantum efficiency of UV detectors at shorter wavelengths. Hosseini & Sahai (2019) find that AMUSS, coupled to a 30 cm space-based telescope, can obtain a spectrum (with 10 km s^{-1} resolution) in a limited bandpass[19] of (say) $\sim(1600–1620)$ Å, of an astrosphere that is as faint as the faintest source in our survey, RW Boo, with about 5 hr of integration time per source, and detect the 1610 Å line with $\gtrsim 5\sigma$. RW Boo has a flux of 1 cps, i.e., a factor ~ 10 less than IRC+10216 in an elliptical aperture with area A_{shs} covering the brightest part of its astrosphere. For comparison, the brightest source in our survey, U Ant, has a flux of 5.5 cps in an elliptical aperture with area A_{shs}, covering the brightest part of its astrosphere.

6. Conclusions

Using the GALEX archive, we have discovered extended structures around a small sample of AGB stars emitting in the FUV band.

1. In nine out of ten objects, we find the typical morphology expected for a spherical wind moving relative to, and interacting with, the ISM to produce an astrosphere (including one tentative detection). The exception is the carbon star, V Hya, whose mass-ejection is known to be highly aspherical; in it we find evidence of its large parabolic high-velocity outflows interacting with the ISM and its collimated, extreme velocity outflows interacting with the circumstellar medium.
2. W Hya shows a complex morphology with multiple azimuthal and radial structures, in addition to its astrosphere.
3. For eight objects with relatively large proper motions, we find (as expected) that the termination-shock region lies in a hemisphere that contains the proper motion vector. For five out of eight objects (EY Hya, RT Vir, R Hya, RW Boo, and RX Boo) the symmetry axis of the termination shock lies within $\lesssim \pm 30°$ of the proper motion vector. One object (R LMi), which has a very small proper motion by far, compared to the others, shows a roughly circular morphology for its astrosphere.

4. Radial intensity cuts for each source, averaged over large azimuthal wedges, locate the termination shock, the astropause and its outer edge. In a few objects, the cuts also reveal faint emission just outside the astropause that likely arises in shocked ISM material.
5. The radii of the termination shock and the width of the astropause derived from the intensity cuts, together with published mass-loss rates and wind expansion velocities, have been used to determine the total mass lost and mass-loss duration for each source—we find that the duration of, and total mass in, the shocked wind are significantly larger than their corresponding values for the unshocked wind.
6. The total derived ejecta masses for all eight stars with well-detected astrospheres are small (or very small) fractions of the minimum mass that needs to be lost before such stars enter the post-AGB evolutionary phase.
7. The NUV images of these objects do not show the extended emission structures, indicating that the FUV emission is due to H$_2$ Lyman–Werner band lines within the wide GALEX FUV filter bandpass, excited by collisions with hot electrons produced as a result of the shock interaction, as has been hypothesized for other astrospheres detected in FUV emission. We derive a model spectrum of the FUV emission from a representative bright region in the astrosphere of IRC+10216, assuming it results from this mechanism.
8. We show that a Spatial Heterodyne Spectrometer instrument, mounted on a relatively small-aperture space-based telescope, can obtain high-velocity resolution spectra of the faint FUV emission from astrospheres around AGB stars in 5 hr or less per source in order to confirm (or refute) the origin of this emission as resulting from H$_2$ Lyman–Werner band lines.

Appendix

The following table (Table 4) lists all AGB stars for which GALEX images were examined in order to search for extended UV emission associated with the stars but where no such emission was found. The root names of the image fits files for these sources, together with the exposure times, Galactic coordinates, distance, height above the Galactic plane, and FUV extinction, are listed.

---

[19] Since the noise in a spectrum obtained with AMUSS varies as the square root of the total bandpass, it is advantageous to limit the bandpass as much as possible while still being able to detect the line(s) of interest.

Table 4
AGB Stars without Extended UV Emission

Name (Simbad)	Sp.Typ.	Image Root Name	Exp.Time (s)	Long. (deg)	Lat. (deg)	Dist. (kpc)	z (kpc)	A_{FUV}
TT Peg	M3	GI4_042001_AOHI000702p270035	1613	110.7468	−34.7159	0.716	−0.408	0.28
AG Cet	M5III	GI1_026004_Arp100	1593.05	102.2252	−73.5815	0.279	−0.268	0.14
TU And	M6e	GI1_023001_HIP2546	1611	117.5941	−36.6447	1.010	−0.603	0.26
TW Psc	M8	MISDR1_16795_0418	1658	118.6546	−48.5745	0.713	−0.535	0.20
57 Psc	M4IIIa	MISDR1_16810_0419	1648	121.1921	−47.3799	0.220	−0.162	0.32
CR Cet	M4III	MISWZS01_29157_0269	2415.35	128.2863	−64.4344	0.329	−0.297	0.31
Z Psc	C	GI1_023021_ZPsc	3368.4	129.8623	−36.7705	0.622	−0.372	0.52
AA Tri	M3	NGA_NGC0777	1971.9	139.3226	−29.6082	0.199	−0.098	0.29
R Cet	M4−5e	GI1_037003_J022604p002135	6019.8	166.9656	−54.7512	0.633	−0.517	0.36
X For	M3	MIS2DFSGP_28387_0161	1658.1	217.0063	−65.1053	0.964	−0.875	0.16
RR Eri	M5III	MISDR1_18658_0457	1696	185.1699	−55.7683	0.375	−0.310	0.35
X Cet	M5.5e	MISGCSS_18775_0410	3375.4	182.9203	−45.9836	1.517	−1.091	0.42
GL Eri	M5III	GI1_047021_ESO302_G014	1696	242.3073	−51.0352	0.309	−0.240	0.18
V Eri	M5/M6IV	GI1_023013_HIP19004	1616	208.8489	−43.9775	0.297	−0.207	0.19
BD−05 836	M5	MISDR1_26911_0465	3157.95	196.5405	−37.9160	0.668	−0.410	0.51
V Cam	M7	GI1_023023_VCam	2300	139.3941	22.8971	0.627	0.244	1.13
HD 45819	M5III	GI1_099014_NGC2249	1531.25	278.8037	−27.6048	0.705	−0.327	0.35
AA Cam	M5S	GI1_023002_HIP35045	1693	146.7974	27.2566	0.475	0.218	0.91
VX Aur	M4	GI4_016002_DDO43	1688	177.6081	24.0286	1.018	0.414	1.13
EY Cam	M5	GI3_061009_UGCA133	1693.05	148.4479	29.1185	0.519	0.253	0.89
Y Gem	M8	MISGCSAN_15326_2078	1531.05	199.4917	19.7929	0.644	0.218	1.23
SV Lyn	M5III:	MISGCSAN_04353_0757	1522.1	184.5586	29.5006	0.244	0.120	0.50
RZ UMa	M8	GI1_023003_HIP40060	1616	150.8722	32.7450	0.509	0.275	0.81
RX Cnc	M8	MISGCSAN_15612_1585	1701.05	198.0768	28.5631	0.522	0.250	0.90
RY Hya	Ce	MISGCSAN_16455_1184	1703	220.8651	20.9410	1.469	0.525	0.65
Z Cnc	M6III	GI4_042008_AOHI082329p150918	1639.05	209.0836	26.7663	0.419	0.189	0.44
FW Cnc	M0	MISGCSAN_16578_1760	2931.25	216.8179	30.7204	0.365	0.187	0.38
S Hya	M4−M6.5e	MISWZN09_24230_0565	3156.05	224.9863	28.4174	1.116	0.531	0.49
FZ Cnc	M4IIIv	GI1_113005_SY_CNC	4794.35	209.5405	36.1078	0.221	0.130	0.24
HD 77938	M4/M5III	GI2_023004_T_PYX	880	257.2315	9.6299	0.327	0.055	0.45
NR Hya	M8	MISDR1_24351_0470	3174.05	230.8246	29.0731	0.662	0.322	0.47
CW Cnc	M6	MISGCSAN_23934_2434	1682.1	216.2250	36.2926	0.252	0.149	0.29
IN Hya	M3	MISWZN09_24315_0213o	1686.05	231.9017	32.7302	0.327	0.177	0.34
DF Leo	M4III	MISDR3_24067_1195	1689.05	224.4304	37.1814	0.327	0.197	0.32
TW Sex	M4	MISDR1_24339_0267	3041.15	238.3158	39.6127	0.452	0.288	0.35
UY Leo	M7III:	GI1_047040_UGC05672	1766.1	212.1644	57.6836	0.715	0.605	0.26
S Sex	M4−5e	MISDR1_24330_0273	1690.1	247.2382	47.2226	1.353	0.993	0.30
GV UMa	M5	LOCK_08	12087.3	152.2240	52.5242	0.568	0.451	0.55
R UMa	M5−8e	GI1_023015_HIP52546	1703	138.3629	44.3614	0.560	0.391	0.64
VY UMa	C	GI1_023025_VYUma	1704	139.5897	45.4137	0.416	0.296	0.61
GY UMa	M4III	GI4_016006_DDO87	1533.05	141.0463	46.9199	0.307	0.225	0.55
56 Leo	M5.5III	MISWZN11_12423_0315	1533.05	245.0495	55.4968	0.115	0.095	0.09
FF Leo	M5	MISWZN11_12490_0416	954.55	249.4775	55.3027	0.858	0.705	0.27
AK Leo	M...	GI5_039002_AGC215158_HA1	1585.15	249.8324	68.3165	0.648	0.602	0.23
R Com	M5−7e	GI1_079001_NGC4064	1691.05	248.0329	76.3160	1.261	1.225	0.22
FZ Vir	M...	MISDR1_13708_0334	1513.5	291.7645	59.9583	0.402	0.348	0.25
T CVn	M5	GI4_015003_DDO133	9973.5	168.2676	83.6332	0.800	0.795	0.43
BZ Vir	M5	GI1_047084_UGCA319	1462	306.0581	45.1690	2.486	1.763	0.32
SY CVn	M8	GI1_047086_UGC08215	1572.2	113.6014	69.7432	0.760	0.713	0.23
FH Vir	M6III	GI1_023005_HIP64768	1665.1	320.1010	68.5401	0.359	0.334	0.23
RW CVn	M7III:	GI1_026018_Arp84	2811.4	72.2044	72.4610	0.462	0.441	0.23
BY Boo	M4.5:III	MISGCSN_01277_1394	1222.1	85.2586	67.2613	0.166	0.153	0.15
FS Vir	M4III	MISDR1_33714_0583	1690.1	346.5112	58.9557	0.248	0.213	0.21
NO Vir	M5	MISWZN15_33932_0237	1575.95	342.8404	53.3535	0.497	0.399	0.28
AO Vir	M4	MISDR1_33712_0584	2504.1	349.7972	58.2956	3.514	2.990	0.26
S Boo	M5−6e	PS_GROTH_MOS01	4048.35	96.9253	58.4554	1.595	1.359	0.26
RS Vir	M8	MISWZN15_33657_0360o	1630	352.6741	57.9715	0.453	0.384	0.26
NV Vir	M5III	MISWZN15_33963_0340	1942.1	348.2470	49.3709	0.773	0.587	0.30
NU Aps	M5III	GI4_099003_IC4499	4295.9	306.8874	−20.7643	0.600	−0.213	0.46
Y Ser	M5e	MISWZN15_33920_0338	2493.2	358.4771	45.0585	0.436	0.309	0.32
Z Ser	M5	MISDR1_33757_0591	1668.05	3.3780	47.3378	0.907	0.667	0.31
Y CrB	M8III:	GI1_023007_HIP77284	2883.1	61.3352	51.8605	0.686	0.539	0.29
X Her	M8	GI5_021006_X_Her	3024.1	74.4645	47.7858	0.123	0.091	0.09

Table 4
(Continued)

Name (Simbad)	Sp.Typ.	Image Root Name	Exp.Time (s)	Long. (deg)	Lat. (deg)	Dist. (kpc)	z (kpc)	A_{FUV}
FQ Ser	M3	MISGCSAN_22074_1730	1645.05	20.8265	39.9553	0.180	0.116	0.18
RU Her	M6−7e	GI1_023008_HIP79233	2426.7	41.9779	45.6111	0.684	0.489	0.32
TV Dra	MS	MISDR1_09998_0349	2584	94.3435	35.3483	0.510	0.295	0.39
V945 Her	M5	MISDR2_22240_0978	2717.05	53.6682	32.1726	1.372	0.731	0.45
T Dra	Nev	GI1_023020_HIP87820	1612.45	86.7498	29.9422	0.944	0.471	0.47
SS Lyr	M5IIIe	GI4_056015_KEPLER_06	5800.05	77.9802	16.0017	0.748	0.206	0.81
GY Aql	M8	GI1_023009_HIP97586	2608.25	32.7232	−16.4858	0.706	−0.200	0.59
UX PsA	M3/M4III	MIS2DFSGP_40469_0326	1527.1	16.7881	−48.0706	0.397	−0.295	0.20
TU Peg	M7−8e	MISDR2_20095_0732	1937.2	68.2077	−29.7630	0.620	−0.308	0.33
EP Aqr	M8IIIv	MISWZS22_20562_0261	2759	54.2001	−39.2604	0.133	−0.084	0.08
KL Aqr	M8	MISGCSN_20728_0261o	2279.3	59.7637	−41.2647	0.505	−0.333	0.24
SV Peg	M7	GI1_023010_HIP109070	1724.05	88.7152	−16.2856	0.401	−0.113	0.44
TX Peg	M...	MISDR2_20490_0736	1687.15	75.7147	−34.8694	0.550	−0.314	0.28
S Gru	M8IIIe	GI1_047110_ESO238_G005	2415.2	345.8846	−54.7673	0.561	−0.458	0.18
AF Peg	M5II−III	GI1_023011_HIP112868	1646.9	86.8368	−36.2020	0.402	−0.238	0.26
TY And	M...	GI1_023012_HIP114757	1887	103.8529	−18.4676	0.662	−0.210	0.50
SV Aqr	M8	MISDR1_29581_0645	2733.05	66.6906	−63.5235	0.422	−0.378	0.16
LW Aqr	M4III	MISWZS00_29619_0271	1690.25	77.7709	−69.5664	0.405	−0.379	0.15
XZ Psc	M5III	MISWZS00_29073_0165	4289.4	94.0594	−59.5482	0.180	−0.155	0.12

ORCID iDs

Raghvendra Sahai ● https://orcid.org/0000-0002-6858-5063

References

Amôres, E. B., Jesus, R. M., Moitinho, A., et al. 2021, MNRAS, 508, 1788
Amôres, E. B., & Lépine, J. R. D. 2005, AJ, 130, 659
Andriantsaralaza, M., Ramstedt, S., Vlemmings, W. H. T., et al. 2022, A&A, 667, A74
Bailer-Jones, C. A. L., Rybizki, J., Fouesneau, M., et al. 2021, AJ, 161, 147
Bianchi, L. 2011, Ap&SS, 335, 51
Blondin, J. M., & Koerwer, J. F. 1998, NewA, 3, 571
Brown, D., & Bomans, D. J. 2005, A&A, 439, 183
Coşkunoğlu, B., Ak, S., Bilir, S., et al. 2011, MNRAS, 412, 1237
Comeron, F., & Kaper, L. 1998, A&A, 338, 273
Corliss, J. B., Harris, W. M., Mierkiewicz, E. J., & Roesler, F. L. 2015, ApOpt, 54, 8835
Cox, N. L. J., Kerschbaum, F., van Marle, A.-J., et al. 2012, A&A, 537, A35
Danilovich, T., Teyssier, D., Justtanont, K., et al. 2015, A&A, 581, A60
Dawson, O. R., & Harris, W. M. 2009, ApOpt, 48, 4227
De Beck, E., Decin, L., de Koter, A., et al. 2010, A&A, 523, A18
Decin, L., Cox, N. L. J., Royer, P., et al. 2012, A&A, 548, A113
Dgani, R., van Buren, D., & Noriega-Crespo, A. 1996, ApJ, 461, 372
Díaz-Luis, J. J., Alcolea, J., Bujarrabal, V., et al. 2019, A&A, 629, A94
Gaensler, B. M., Madsen, G. J., Chatterjee, S., & Mao, S. A. 2008, PASA, 25, 184
Gaia Collaboration 2022, yCat, I/355
Harlander, J., Reynolds, R. J., & Roesler, F. L. 1992, ApJ, 396, 730
Hosseini, S. 2019, ApOpt, 58, 2311
Hosseini, S., & Harris, W. 2020, JATIS, 6, 015005
Hosseini, S., & Harris, W. M. 2012, Proc. SPIE, 8146, 814617
Hosseini, S., & Sahai, R. 2019, in IAU Symp. 355, The Realm of the Low Surface Brightness Universe (Tenerife: IAU)
Izumiura, H., Ueta, T., Yamamura, I., et al. 2011, A&A, 528, A29
Izumiura, H., Water, A. M., Loup, C., et al. 1997, A&A, 323, 449
Jura, M. 1986, ApJ, 303, 327
Kalberla, P. M. W., & Kerp, J. 2009, ARA&A, 47, 27
Kastner, J. H., & Wilson, E. 2021, ApJ, 922, 24
Kerschbaum, F., Ladjal, D., Ottensamer, R., et al. 2010, A&A, 518, L140
Kerschbaum, F., Maercker, M., Brunner, M., et al. 2017, A&A, 605, A116
Knapp, G. R., Jorissen, A., & Young, K. 1997, A&A, 326, 318
Kobulnicky, H. A., Schurhammer, D. P., Baldwin, D. J., et al. 2017, AJ, 154, 201
Krtička, J. 2014, A&A, 564, A70
Liu, W., & Dalgarno, A. 1996a, ApJ, 462, 502
Liu, W., & Dalgarno, A. 1996b, ApJ, 467, 446
Maercker, M., Khouri, T., Mecina, M., et al. 2022, A&A, 663, A64
Martin, D. C., Seibert, M., Neill, J. D., et al. 2007, Natur, 448, 780
Matthews, L. D., Gérard, E., & Le Bertre, T. 2015, MNRAS, 449, 220
Matthews, L. D., Le Bertre, T., Gérard, E., & Johnson, M. C. 2013, AJ, 145, 97
Matthews, L. D., Libert, Y., Gérard, E., et al. 2008, ApJ, 684, 603
Mauron, N., & Huggins, P. J. 2006, A&A, 452, 257
Mauron, N., Huggins, P. J., & Cheung, C.-L. 2013, A&A, 551, A110
Mierkiewicz, E. J., Reynolds, R. J., Roesler, F. L., et al. 2006, ApJL, 650, L63
Mierkiewicz, E. J., Roesler, F. L., Harlander, J. M., Reynolds, R. J., & Jaehnig, K. P. 2007, Optica Publishing Group, paper JWA1, https://opg.optica.org/abstract.cfm?URI=HISE-2007-JWA1
Miller Bertolami, M. M. 2016, A&A, 588, A25
Mohamed, S., Mackey, J., & Langer, N. 2012, A&A, 541, A1
Morrissey, P., Schiminovich, D., Barlow, T. A., et al. 2005, ApJL, 619, L7
Olofsson, H. 2008, PhST, 133, 014028
Olofsson, H., González Delgado, D., Kerschbaum, F., et al. 2002, A&A, 391, 1053
Olofsson, H., Maercker, M., Eriksson, K., et al. 2010, A&A, 515, A27
Peri, C. S., Benaglia, P., & Isequilla, N. L. 2015, A&A, 578, A45
Ramstedt, S., Vlemmings, W. H. T., Doan, L., et al. 2020, A&A, 640, A133
Saberi, M., Vlemmings, W. H. T., & De Beck, E. 2019, A&A, 625, A81
Sahai, R. 1990, ApJ, 362, 652
Sahai, R., & Chronopoulos, C. K. 2010, ApJL, 711, L53
Sahai, R., Huang, P.-S., Scibelli, S., et al. 2022, ApJ, 929, 59
Sahai, R., & Mack-Crane, G. P. 2014, ApJ, 787, 40
Sahai, R., Morris, M. R., & Villar, G. G. 2011, AJ, 141, 134
Sahai, R., Scibelli, S., & Morris, M. R. 2016, ApJ, 827, 92
Sahai, R., & Trauger, J. T. 1998, AJ, 116, 1357
Scibelli, S., Sahai, R., & Morris, M. R. 2019, ApJ, 870, 117
Smith, N. 2014, ARA&A, 52, 487
Ueta, T. 2008, ApJL, 687, L33
Ueta, T., Izumiura, H., Yamamura, I., et al. 2008, PASJ, 60, S407
Ueta, T., Speck, A. K., Stencel, R. E., et al. 2006, ApJL, 648, L39
Ueta, T., Stencel, R. E., Yamamura, I., et al. 2010, A&A, 514, A16
van Buren, D., & McCray, R. 1988, ApJL, 329, L93
van Leeuwen, F. 2007, A&A, 474, 653
Villaver, E., Manchado, A., & García-Segura, G. 2012, ApJ, 748, 94
Vishniac, E. T. 1994, ApJ, 428, 186
Wareing, C. J., Zijlstra, A. A., & O'Brien, T. J. 2007, ApJL, 660, L129
Watchorn, S., Roesler, F. L., Harlander, J., et al. 2010, ApOpt, 49, 3265